



Application of Operando X-ray Diffraction and Raman Spectroscopies in Elucidating the Behavior of Cathode in Lithium-Ion Batteries

Wen Zhu¹, Dongqiang Liu², Andrea Paoletta², Catherine Gagnon², Vincent Gariépy², Ashok Vijn¹ and Karim Zaghib^{2*}

¹ IREQ-Hydro Québec, Varennes, QC, Canada, ² Centre d'Excellence en Électrification des Transports et Stockage d'Énergie, Varennes, QC, Canada

OPEN ACCESS

Edited by:

Verónica Palomares,
University of the Basque Country
(UPV/EHU), Spain

Reviewed by:

Zhixiang Shi,
Southeast University, China
Xifei Li,
Xi'an University of Technology, China

*Correspondence:

Karim Zaghib
zaghib.karim@ireq.ca

Specialty section:

This article was submitted to
Energy Storage,
a section of the journal
Frontiers in Energy Research

Received: 28 February 2018

Accepted: 19 June 2018

Published: 31 July 2018

Citation:

Zhu W, Liu D, Paoletta A, Gagnon C,
Gariépy V, Vijn A and Zaghib K (2018)
Application of Operando X-ray
Diffraction and Raman
Spectroscopies in Elucidating the
Behavior of Cathode in Lithium-Ion
Batteries. *Front. Energy Res.* 6:66.
doi: 10.3389/fenrg.2018.00066

With the advances in characterization techniques, various operando/in-situ methods were applied in studying rechargeable batteries in order to improve the electrochemical properties of electrode materials, prolonging the battery life and developing new battery materials. In the present review, we focus on the characterization of electrode materials with operando/in-situ X-ray diffraction and Raman spectroscopies. By correlating the results obtained via these two techniques in different electrode chemistry: (a) intercalation materials, such as layered metal oxides and (b) conversion materials, such as elemental sulfur. We demonstrate the importance of using operando/in-situ techniques in examining the microstructural changes of the electrodes under various operating conditions, in both macro and micro-scales. These techniques also reveal the working and the degradation mechanisms of the electrodes and the possible side reactions involved. The comprehension of these mechanisms is fundamental for ameliorating the electrode materials, enhancing the battery performance and lengthening its cycling life.

Keywords: operando/in-situ XRD, operando/in-situ Raman, lithium-sulfur, layered metal oxide, LiFePO₄, spinel oxide

INTRODUCTION

Rechargeable batteries are the main energy source for electric vehicles (EV), consumer electronics, and promising candidates for renewable energy storage, owing to their relative high energy and power densities, light weight, long cycle life and environmental acceptability (Tarascon and Armand, 2001; Palacín, 2009; Dunn et al., 2011; Budde-Meiwes et al., 2013). For the large-scale commercialization of EVs and the utilization of renewable energy, the energy storage capacity, cycle life, rate capacity and safety of most commercial batteries still need to be improved (Armand and Tarascon, 2008; Etacheri et al., 2011; Wen et al., 2012). To achieve these goals, the scientific community is devoting a major effort to improve the existing materials and identify new ones to meet these requirements.

Among the many rechargeable battery materials, the layered oxide family of LiMeO₂ (Me = Ni, Co, Mn, and their mixtures) has been widely studied. These oxides yield high specific

energy and/or power, and structural and thermal stability, as well as long cycling life (Hwang et al., 2003; Hu et al., 2009; Huang et al., 2011; Park et al., 2012; Liao et al., 2016; Berckmans et al., 2017), but they still suffer from poor rate capability, especially at high C-rates (Chen et al., 2016b). Spinel $\text{Li}(\text{Mn},\text{Ni})_2\text{O}_4$ (LMN) is of great interest due to its high working voltage and high energy density, relatively low cost and environmentally benign. However, its fast capacity fade at elevated temperatures makes it unsuitable for practical applications (Amine et al., 1996; Ohzuku et al., 1999; Goodenough and Kim, 2010; Yang et al., 2013; Julien et al., 2014). Olivine structured LiFePO_4 (LFP) is another promising cathode with reasonable high capacity, superior cycle life, structural and thermal stability, low cost, high safety and non-toxicity. However, its low operating voltage and low conductivity limit its wide applications (MacNeil et al., 2002; Sarkar and Mitra, 2014; Zhao et al., 2016). In addition to the Li-ion families mentioned above, Li-sulfur and Li-air batteries are also being intensively investigated owing to their high theoretical capacities, low cost and environmentally benign. Unfortunately, the present performance of both Li-S and Li-air batteries, such as energy density, rate capability, cyclability, Li-metal fading and safety, are unable to satisfy the requirements of commercial applications (Girishkumar et al., 2010; Ji and Nazar, 2010; Mikhaylik et al., 2010; Kraysberg and Ein-Eli, 2011; Manthiram et al., 2013; Yang et al., 2018).

To further improve the performance of the batteries already present in the market, such as those based on LiCoO_2 (LCO), $\text{Li}(\text{Ni},\text{Co},\text{Mn})\text{O}_2$, and LFP cathodes, it is essential to have a clear picture of the working and failure mechanisms of these batteries. Various ex-situ materials characterization techniques, such as X-Ray Diffraction (XRD), X-ray Absorption Spectroscopy (XAS), X-ray computed tomography (micro CT) (Carter et al., 2018), neutron diffraction, neutron magnetic resonance (NMR) (Ogata et al., 2014), Raman spectroscopy, Fourier-Transform Infrared (FTIR), Ultraviolet and Visible (UV-Vis) spectroscopy, Scanning and Transmission Electron Microscopies (SEM, TEM) etc. are employed to investigate the pristine and cycled electrodes at both macro and atomic scales. However, these ex-situ analyses cannot provide real-time information of the electrodes during cycling, which is crucial for understanding the working and degradation mechanisms of the batteries. In recent years, operando and in-situ (operando and in-situ will be used interchangeably hereafter) characterization techniques have been advanced and widely applied in following the real-time situation of electrodes in batteries under various operating conditions. Operando XRD is used to investigate the phase transformation and crystal structure changes of electrodes during cycling (Yang et al., 2002; Yang and Nam, 2010; Sun et al., 2013; Zhang et al., 2014; Zhu et al., 2014; Wang and Wang, 2016). Neutron diffraction is also applied to study the structure and phase developments in cycling cells (Wang et al., 2012; Bobrikov et al., 2014, 2017; Dolotko et al., 2014; Li et al., 2015) because it is more sensitive to the light elements (such as lithium) as compared to XRD, an important issue in understanding the behavior of lithium in Li-ion batteries. Operando XAS is employed to probe the changes in the local environment of a cation and its electronic structure in relation to the electrochemical processes

happening on electrode surfaces (Chan et al., 2006; Dominko et al., 2009; Giorgetti, 2013; Menzel et al., 2013; Fehse et al., 2014; Giuliana et al., 2017). The absorption spectrum is divided into the X-ray Absorption Near-Edge Structure (XANES) region and the Extended X-ray Absorption Fine Structure (EXAFS) region; the former examines the oxidation state, coordination number, electronic configuration and site symmetry, whereas the latter provides information on average interatomic distances. Raman spectroscopy is also used to explore the variation in the local structure and oxidation state, as well as the thermal stability of electrode surfaces or electrode-electrolyte interfaces during charge-discharge and heat treatment (Dokko et al., 2002; Hardwick et al., 2008; Membreno et al., 2013; Stancovski and Badilescu, 2013; Wu et al., 2013); FTIR is another effective tool for studying the surface and evolution of electrode-electrolyte interfaces under cell operating conditions (Aurbach and Chusid, 1997; Chusid et al., 2001; Cheng et al., 2007; Ye et al., 2016). In addition to these spectroscopic techniques, operando SEM (Miller et al., 2013; Hovington et al., 2014; Marceau et al., 2016) and TEM (Liu, S. et al., 2014; Janish and Carter, 2015; Wang, 2015; Chen et al., 2016a; Xu et al., 2016) show the evolution of direct images of cycling electrode at the micro- and nano-scales. By combining the images with energy dispersive X-ray spectroscopy, electron energy loss spectroscopy and electron diffraction, the information on particle morphology, crystal structure, phase transformation, multi-phase interface behavior, element distribution and element positions are obtained as a function of the electrochemical process. In short, operando measurements or multi-operando measurements reveal indispensable information on how the electrodes behave and how their structures change under working conditions. These insights enable researchers to correlate the electrochemical process with the crystal structure, composition, oxidation state of ions and stresses etc. at both macro- and micro-scales, which are essential to understand the operation and failure mechanisms of batteries. The outcome of this effort is to identify new solutions being able to improve the performance of electrodes to meet the requirements for electric vehicles and storage of renewable electrical energy. Ideally the best operando techniques must be non-invasive and performed under real battery cycling. Among all the possibilities, operando X-ray diffraction is the most widely used due to the instrument availability, simple cell design, examining “bulk” material and most importantly, revealing the information on crystal structure, phase transformation as well as stresses, etc.; whereas operando TEM involves complicated cell design; testing conditions are far from real operating conditions; damage of the analyzed materials and decomposition of the liquid electrolyte are often induced due to intense electron beam used, but the technique provides information on the structural morphological changes in nano-scale. On the other hand, operando XAS and Raman techniques are also used to study the local structure of the electrode materials, but unfortunately the former need to be performed with synchrotron radiation source which is not accessible to many researchers whereas Raman spectrometer is widely available in many research facilities. In the present work, we focus on the applications of XRD and Raman to

four types of electrodes, i.e., LCO, LMN, LFP and elemental sulfur. We demonstrate the contribution of these techniques to the fundamental comprehension of electrode behavior under operating conditions that are critical for raising the capacity and life span of the batteries from the current state.

METHODS

The Operando X-ray Diffraction

The operando XRD, both reflection and transmission modes are used to monitor crystal structure and phase changes of electrodes during battery cycling. Different in-situ cell configurations were designed (Li et al., 1993; Leriche et al., 2010; Zhu W. et al., 2013; Roberts et al., 2014; Bleith et al., 2015) with an x-ray transparent window, such as a beryllium disk (Reimers and Dahn, 1992; Ma et al., 2013; Cañas et al., 2017), polymer films (Kapton, Mylar) (Mohanty et al., 2013; Sun et al., 2013) and aluminum foil (Zhu W. et al., 2013; Roberts et al., 2014). A beryllium window has the advantages of maintaining contact between cell components and is nearly 100% x-ray transparent due to disk rigidity and low x-ray absorption. However, beryllium corrosion was observed, especially at high voltage >4.2 V (Reimers and Dahn, 1992; Morcrette et al., 2002). In addition, beryllium is toxic and expensive compared to many other materials. Kapton, Mylar and aluminum are stable, low cost and non-toxic. They also allow X-rays to pass through with certain absorption, but it is difficult to keep cell pressurized with a large area window due to their flexibility. Aluminum foil is used as a current collector in many cases; the same aluminum foil is also used as an x-ray window to reduce undesired diffraction peaks in the spectra. While synchrotron based high-energy X-rays are used, the transmission mode can be applied (Leriche et al., 2010; He et al., 2013; Harks et al., 2015) to follow the evolution of both cathode and anode simultaneously. **Figure 1A** is a schematic diagram of the principle of X-ray diffraction analysis; (**Figure 1a1**) in situ XRD cell design; (**Figure 1a2**) the X-rays diffracted by the atoms on a (hkl) crystal plane satisfying the Bragg's law; (**Figure 1a3**) The information collected by the detector can be expressed as a plot of Intensity vs. d-spacing or 2θ ; (**Figure 1a4**) Determination of the crystal structure from the spectrum; the unit cell size and symmetry can be obtained from peak positions whereas the number of atoms and their positions in the cell depend on the peak intensities.

The Operando Raman Spectroscopy

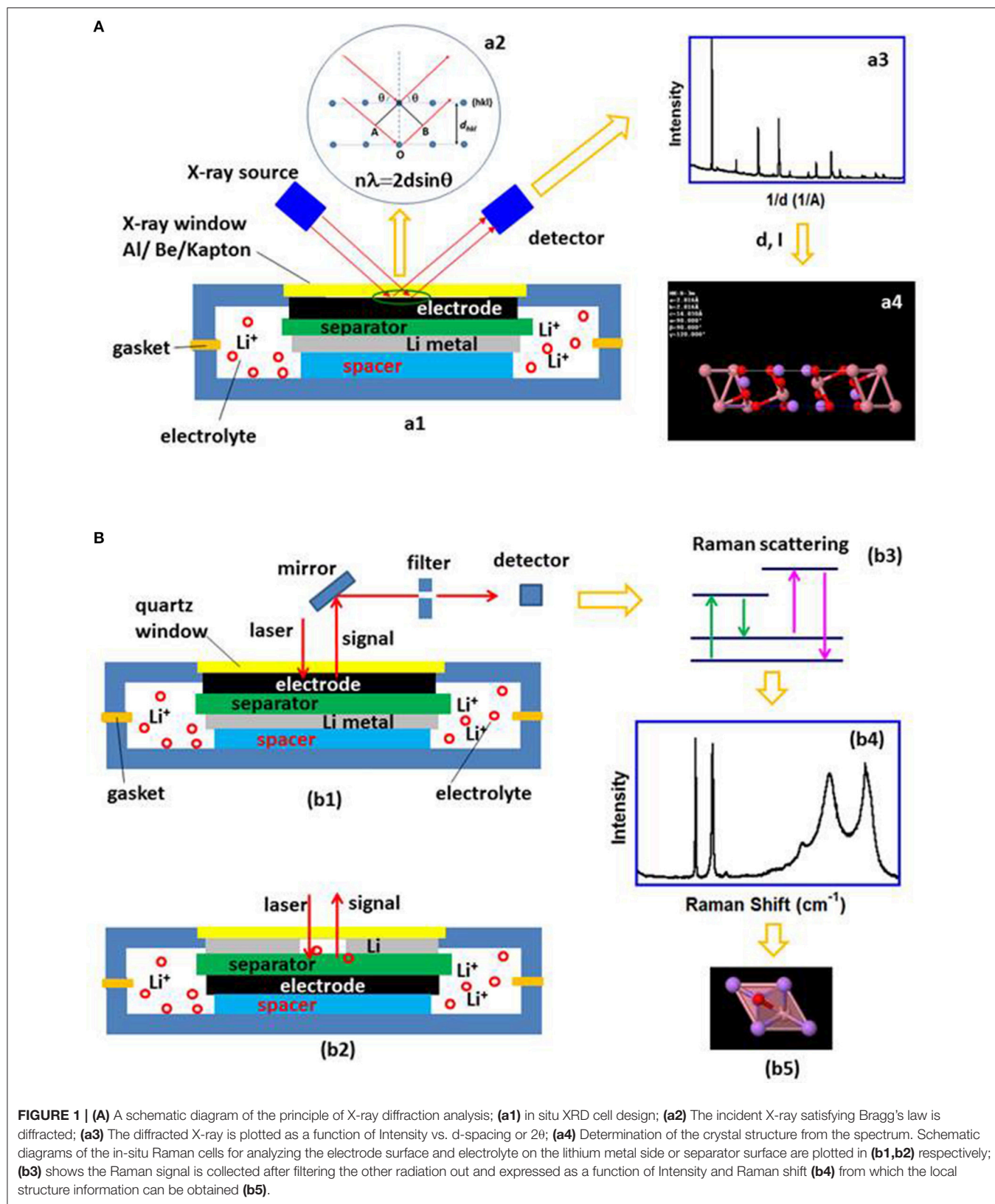
Raman spectroscopy is a technique used to obtain unique structural information at the atomic scale, and it can analyze both solids and liquids. Raman spectroscopy is sensitive to the ion oxidation state and local structure of the material, thus it is useful in monitoring valence and bond change, as well as the corresponding phase transformation of the electrode under operating conditions. The operando Raman cell has a laser-transparent glass window. The cell components can be arranged in different configurations, depending on the components to be examined. Various cell components are amenable to analysis, for example, the changes in the electrodes, the species in the electrolyte on both sides of the separator or changes to the

separator surface (Zhu et al., 2017). **Figures 1b1,b2** show the schematic diagrams of the in-situ Raman cells for analyzing the electrode surface (**Figure 1b1**) and electrolyte on the lithium metal side or separator surface (**Figure 1b2**); (**Figure 1b3**) after filtering the elastic scattered radiation out, the inelastic Raman scattering signal is collected (**Figure 1b3**) and expressed in (**Figure 1b4**) from where the local structure, such as chemical bonds and symmetry, oxidation state of the ions can be obtained (**Figure 1b5**).

THE OPERANDO STUDIES ON CATHODES

LiCoO₂

Layered oxide compounds are the most widely used cathodes for lithium-ion batteries. To achieve high capacity and long life, major effort is focused on understanding the crystal structure change at different stages of charge-discharge, with operando XRD studies making significant contributions in revealing various phase transformations in different cathode materials (Lu and Dahn, 2002; Godbole et al., 2011; Mohanty et al., 2013), especially in the LiCoO₂ family. The operando XRD investigations showed the complicated phase transitions involved in the delithiation of Li_xCoO₂ ($0 \leq x \leq 1$). **Figure 2A** plots the XRD spectra collected during the first charge at rate of C/4.5 in which phases H1, H2, O1a and O1 are observed as a function of cell voltage, where H1 is the fully lithiated phase at $x = 1$ and O1 is the completely delithiated phase at $x = 0$, the others are partially delithiated with $0 < x < 1$. The phase-transformation steps are: H1 → H2 → O1a → O1 (Sun et al., 2001; Chung et al., 2006, 2007). The H1 and H2 have hexagonal lattice in space group (S.G.) $R\bar{3}m$, with similar lattice parameter a , but different in c , $c_{H1} = 14.089$ Å, $c_{H2} = 14.370$ Å respectively (Yang et al., 2000), therefore, the (003) peak shifted to the lower 2θ direction as lattice parameter c increased during the H1 to H2 phase transition; on the other hand, the positions of (101) and (102) are almost unchanged. As the charge voltage reached ~ 4.6 V, (100) and (101) peaks of O1a phase (hexagonal lattice, S.G. $R\bar{3}m$, $a = 2.823$ Å, $c = 27.07$ Å, Chen et al., 2002) appeared and their intensities increased thereafter at the expense of H2 phase. H2 phase completely disappeared as O1 phase started to form, finally, all the O1a phase transformed to O1 phase (hexagonal lattice, $a = 2.83$ Å, $c = 4.24$ Å, S.G.: $P\bar{3}m1$; Amatucci et al., 1996; Yang et al., 2000). A monoclinic phase formed near $x = 0.5$ and other transitional phase, such as H2a, were also detected via operando XRD in different studies under various experimental conditions (Reimers and Dahn, 1992; Ohzuku and Ueda, 1994; Morcrette et al., 2002; Chen and Dahn, 2004). **Figure 2E** is the spectra recorded during the 5th charge to 4.8 V at C/4.5 (Chung et al., 2006). The spectra show no O1 phase formation at the end of charge, instead, the existing phases are O1a and H2 suggesting a delayed phase transformation, which indicates the loss of capacity in the previous cycles. The electrode was further cycled to 8.35 V at C/4.5 during the 12th cycle (not shown here) (Chung et al., 2007). At 4.8 V, the major phases are H1 and H2, O1a was first observed at 5.04 V, and O1a to O1 phase transition completed ~ 6.05 V, which demonstrates the further delayed phase transformation compare to the 5th cycle. After



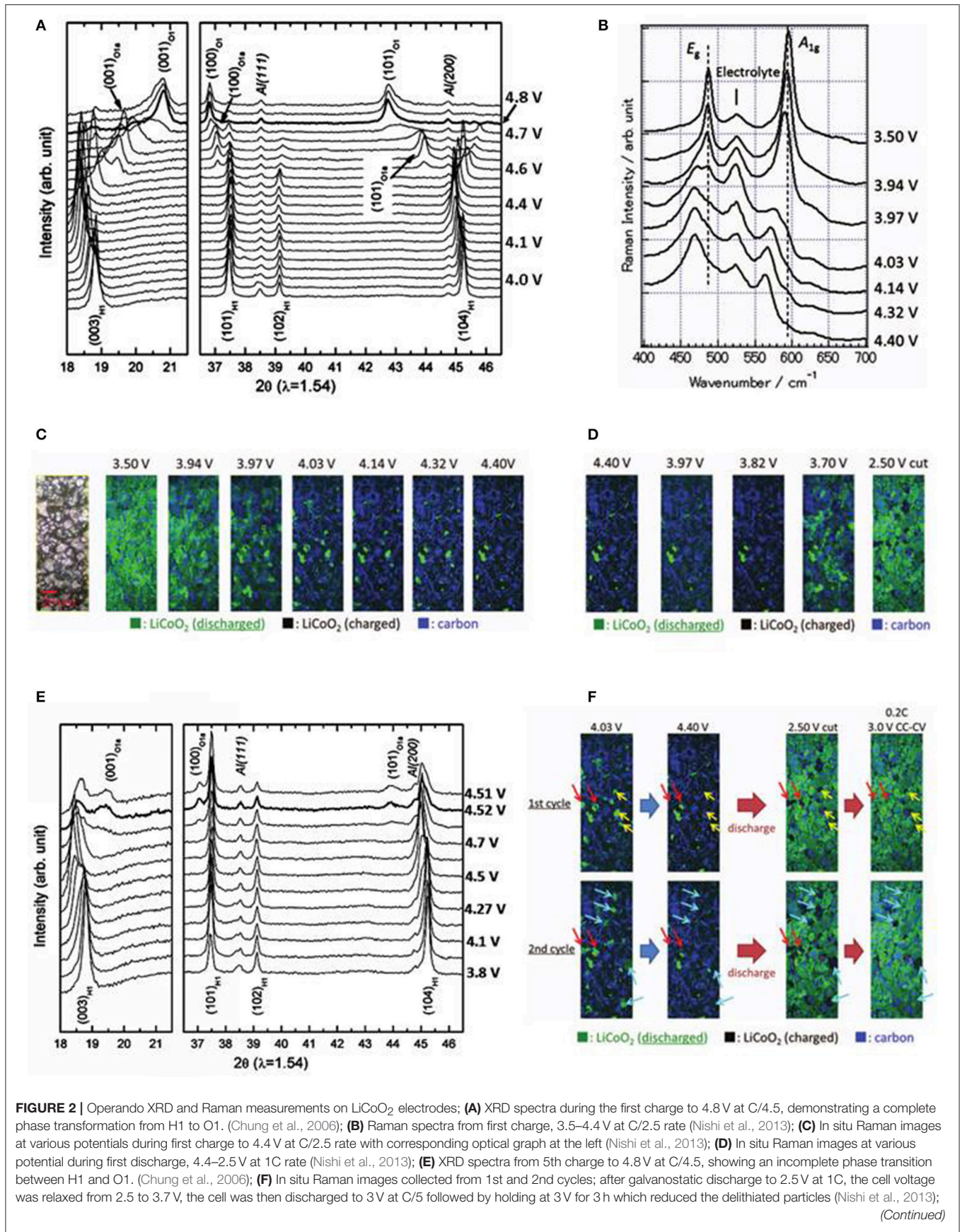


FIGURE 2 | Operando XRD and Raman measurements on LiCo₂ electrodes; **(A)** XRD spectra during the first charge to 4.8 V at C/4.5, demonstrating a complete phase transformation from H1 to O1. (Chung et al., 2006); **(B)** Raman spectra from first charge, 3.5–4.4 V at C/2.5 rate (Nishi et al., 2013); **(C)** In situ Raman images at various potentials during first charge to 4.4 V at C/2.5 rate with corresponding optical graph at the left (Nishi et al., 2013); **(D)** In situ Raman images at various potential during first discharge, 4.4–2.5 V at 1C rate (Nishi et al., 2013); **(E)** XRD spectra from 5th charge to 4.8 V at C/4.5, showing an incomplete phase transition between H1 and O1. (Chung et al., 2006); **(F)** In situ Raman images collected from 1st and 2nd cycles; after galvanostatic discharge to 2.5 V at 1C, the cell voltage was relaxed from 2.5 to 3.7 V, the cell was then discharged to 3 V at C/5 followed by holding at 3 V for 3 h which reduced the delithiated particles (Nishi et al., 2013)

(Continued)

FIGURE 2 | Legends: Red arrows, particles charged and discharged at a slower rate during both cycles; yellow arrows, particles charged at a slower rate in the 1st charge and could not be discharged in the following cycle; blue arrows, particles charged and discharged at a slower rate during the 2nd cycle. Green, black and blue colors in the image represent the discharged LiCoO₂, charged LiCoO₂ and carbon; Panels (A, E) with permission from Elsevier. Panels (B–D, F) with permission from ECS.

the transformation to O1 is completed at 6.05 V, no new phase was found even up to 8.35 V, indicating all Li ions or almost all Li ions are removed from the structure. The charging curves show that the first voltage plateaus are ~ 4.0 , 4.1, and >4.7 V for the 1st, 5th, and 12th cycles respectively, indicating the cell polarization increase caused by the impedance augmentation due to the electrolyte decomposition at high voltage.

The phase transformation mechanism is well-described with the operando XRD results, but the origin of the electrode degradation is still unclear. Therefore, Raman spectroscopy is used to probe the local structure ($\sim \mu\text{m}$ scale) changes of LiCoO₂ (Inaba et al., 1997; Itoh et al., 1997; Nishi et al., 2013; Gross and Hess, 2014) in order to understand the causes of capacity loss. Factorial group analysis indicates that LiCoO₂ has two Raman active modes, A_{1g} and E_g; the former originates from two adjacent oxygen layers moving against each other and parallel to the *c*-axis, whereas the latter is from the atomic displacements perpendicular to the *c*-axis (Baddour-Hadjean and Pereira-Ramos, 2010). The E_g and A_{1g} vibration modes were observed experimentally at 486 and 596 cm⁻¹ (Inaba et al., 1997). **Figure 2B** plots the development of Raman spectra of a LiCoO₂ cathode as the voltage increased from 3.5 to 4.4 V during the first charge. The spectra show: (1) the broadening of E_g and A_{1g} bands due to the formation of shoulder peaks; (2) the shifts of E_g and A_{1g} to the low wave number direction; and (3) the decrease of the band intensities. The appearance of the shoulder peaks on the low wave number side is due to the formation of H2 phase with larger *c*-axis that causes the downward shifts of both bands. At 4.4 V, the E_g and A_{1g} bands contain mainly H2 phase component with a very small H1 phase shoulder, which agrees with the in-situ XRD results. The voltage difference for the first detection of the H2 phase in XRD and Raman measurements reflects the difference between the average particles and individual particle. The band intensity decrease is attributed to the reduced optical skin depth of the incident laser beam due to increasing conductivity from the semiconducting H1 phase transforming to metallic H2 (Inaba et al., 1997). **Figures 2C,D** are the evolutions of Raman images, measured over 180 × 70 μm² with 400 × 150 Raman spectra, during the first charge and discharge respectively, which were constructed using the intensity distributions of the A_{1g} mode of LiCoO₂ and the carbon G band at $\sim 1,600$ cm⁻¹. Starting with fully lithiated LCO (green) at 3.5 V, delithiated LCO (black) formed and grew during charge, eventually reached 94% of the total measured area at 4.4 V, and holding the cell at 4.4 V for an additional 16 h did not delithiate LCO completely ($\sim 2.5\%$ of total measured area remained green), **Figure 1C**. The images show a reversed change, the lithiated areas (green) increase to 90% at 2.5 V when the electrode is discharged at 1C rate (**Figure 1D**). These images illustrate that both charge and discharge rates are significantly different from particle to particle. **Figure 2F** is a comparison of the Raman images of the 1st and 2nd cycles.

Most of the particles were charged and discharged normally, but the behavior of two types of particles directly contributes to the capacity loss: (1) particles were charged at a slower rate in the 1st charge process and could not be discharged in the following cycle (yellow arrows); (2) particles were charged and discharged at a slower rate during the 2nd cycle (blue arrows) resulted in an accumulated delithiated particles of 16% at the end of the 2nd discharge which is more than that of the 1st cycle (10%). The degradation of the electrode with cycling is consistent with the delayed and incomplete phase transformation in comparison of the operando XRD spectra of 1st and 5th cycles (**Figures 2A,E**). After stopping the discharge at 2.5 V, the cell voltage relaxed back to 3.7 V, then was discharged again to 3 V at C/5 and held for 3 h, the delithiated particles were reduced from 10 to 2% for the first cycle (no data was reported for the 2nd cycle). The existence of these “slow” particles is mainly due to the poor local conductivities (Nishi et al., 2013). The operando Raman measurements expose the cause of degradation, i.e., the inhomogeneity of carbon distribution on micrometer scale which makes some particles “slow.” This situation will be aggravated at high cycling rate and after more cycles (Kostecki and McLarnon, 2004). Operando XRD measurements show that phase transformation proceeds progressively, whereas Raman analysis adds details to this progressive transition which is mainly attributed to the reaction speed difference of individual particles caused by local conductivity difference.

LiMn_{1.5}Ni_{0.5}O₄

LiMn_{1.5}Ni_{0.5}O₄ is a high-voltage cathode material with high energy density and low cost, but its cycling stability at high rates needs to be improved for use in practical applications. LiMn_{1.5}Ni_{0.5}O₄ has two different structures, disordered and order, based on the Ni and Mn cation distributions in the LMN. The disordered LMN has a cubic spinel structure with space group Fd $\bar{3}$ m, where the Ni and Mn ions are randomly distributed at the octahedral 16d sites. In contrast, the ordered LMN has the P4₃32 space group, in which the Ni and Mn ions are located in an orderly fashion at the split 4a and 12d sites (Kim et al., 2004; Takahashi et al., 2004; Amdouni et al., 2006). The disordered LMN has better rate capacity because of its higher electric conductivity (Kunduraci et al., 2006) and lithium ions diffusivity (Minami et al., 2005).

The phase evolution during lithium de-intercalation/intercalation of these two structures was studied using in-situ XRD (Kunduraci and Amatucci, 2006; Rhodes et al., 2011; Wang et al., 2011; Hugues et al., 2014; Zhu et al., 2014; Komatsu et al., 2015; Saravanan et al., 2015; Samarasingha et al., 2016) and in situ Raman (Dokko et al., 2002, 2004; Zhu et al., 2015). **Figure 3A** displays the development of the XRD spectra of a Li_xMn_{1.45}Ni_{0.45}Cr_{0.1}O₄ (Cr-LMN) cathode cycled at C/24 with expanded views of peaks (311) and (511) in **Figure 3B**. The initial

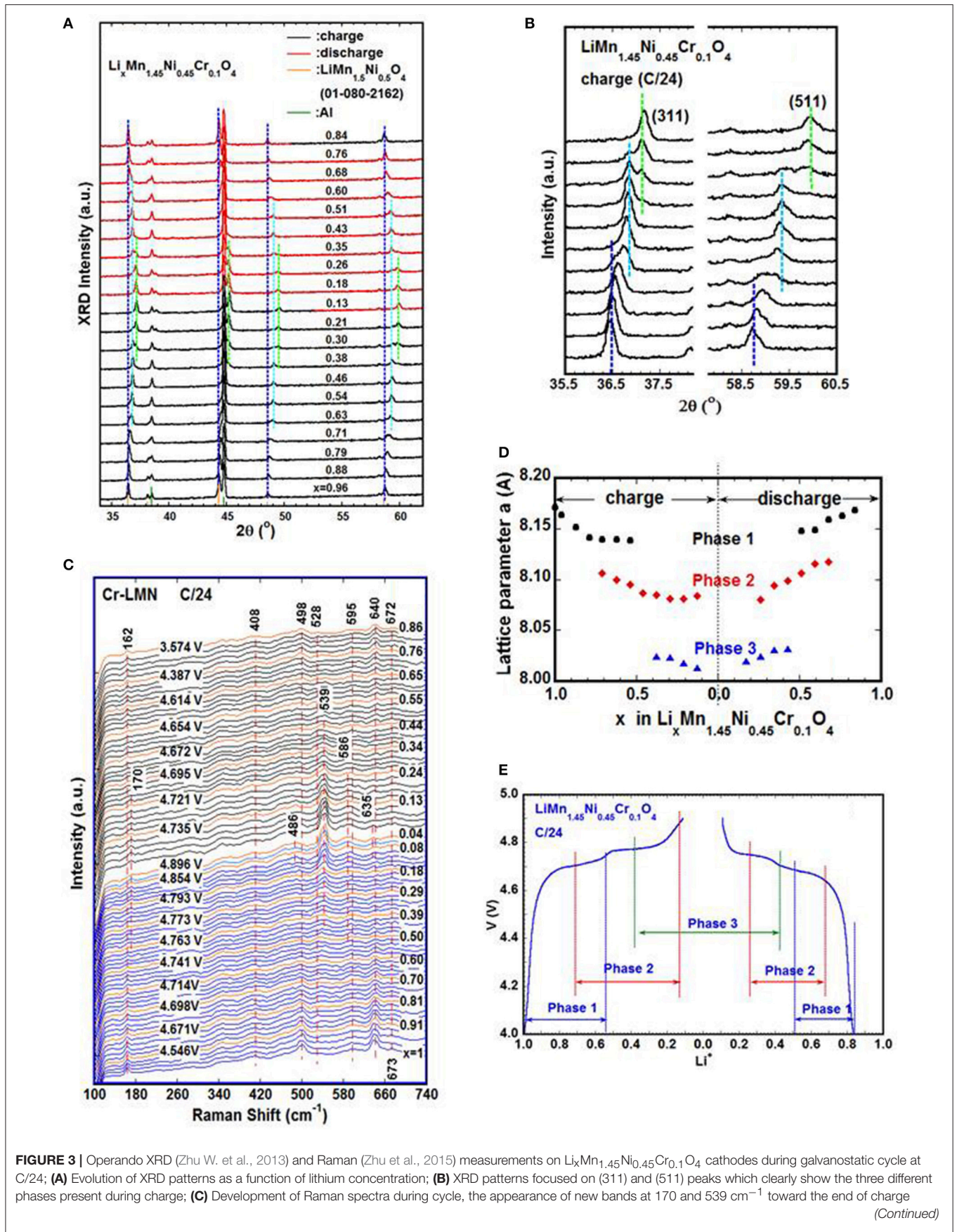


FIGURE 3 | Operando XRD (Zhu W. et al., 2013) and Raman (Zhu et al., 2015) measurements on Li_xMn_{1.45}Ni_{0.45}Cr_{0.1}O₄ cathodes during galvanostatic cycle at C/24; **(A)** Evolution of XRD patterns as a function of lithium concentration; **(B)** XRD patterns focused on (311) and (511) peaks which clearly show the three different phases present during charge; **(C)** Development of Raman spectra during cycle, the appearance of new bands at 170 and 539 cm⁻¹ toward the end of charge
 (Continued)

FIGURE 3 | attributed to the vibration modes of Ni^{4+} -O bond; the two bands are initially observed at ~ 4.76 V corresponding to Phase-3 formation detected by operando XRD. Blue: charge; black: discharge; voltage and x values of orange spectra are labeled; **(D)** Variation of the lattice parameters of different cubic phases in Cr-LMN as a function of Li concentration; **(E)** Relation of cell voltage, lithium concentration and phases determined via operando XRD.

phase is cubic spinel (S.G. $\text{Fd}\bar{3}m$) with $a = 8.177$ Å (Phase-1). All the diffraction peaks shift to higher 2θ angles as the lithium ions are continuously removed from the host structure and two more phases (Phase-2 and Phase-3) form during charge. Upon discharge, the evolution of the spectra changes reversibly. The analysis of the XRD patterns shows that all the phases in the spectra are cubic spinel (S.G. $\text{Fd}\bar{3}m$), and the lattice parameters for each phase as a function of lithium content (x) are obtained from Rietveld refinement of the spectra and plotted in **Figure 3D**. **Figure 3E** shows the variation of the cell voltage with x and the corresponding phases. As charge proceeds from $x = 1$, a solid solution is in the range of $1 \leq x \leq 0.72$; the decrease in Li results only in the decrease of the lattice parameter of the cubic Phase-1. A new cubic spinel phase (Phase-2) starts to emerge and the system entered in a two-phase domain, $0.72 \leq x \leq 0.54$, in which the Phase-2 grows at the expense of the Phase-1 and Phase-1 eventually disappears at $x = 0.54$. Below this concentration, $0.54 \leq x \leq 0.37$, the Cr-LMN is again a solid solution of the Phase-2 only. The system re-enters a two-phase region in the range $0.37 < x < 0.13$ with the coexistence of Phase-2 and a new phase (Phase-3) that grows at the expense of Phase-2. Finally, a solid solution with Phase-3 only is observed in the range $x \leq 0.13$. There is a difference between charge and discharge curves in **Figure 3E** that suggest the thermodynamic equilibrium is not reached even at a slow rate of $C/24$. The off-equilibrium effects evidenced by hysteresis in the structure and electrochemical properties between charge and discharge as a function of x are also linked to its cation disorder (Zhu W. et al., 2013).

While the phase-lithium content relation is determined by operando XRD, the oxidation state of Ni ions is investigated via operando Raman. The vibration modes of Cr-LMN are experimentally detected at $162(\text{T}_{2g}(\text{T}))$, $408(\text{E}_g(\text{Ni}^{2+}/\text{Mn}^{4+}))$, $498(\text{T}_{2g}(\text{Ni}^{2+}))$, $528(\text{T}_{2g}(\text{Ni}^{2+}))$, $593(\text{A}_{1g}(\text{Mn}^{4+}))$, $613(\text{A}_{1g}(\text{Ni}^{2+}))$, $639(\text{A}_{1g}(\text{Mn}^{3+}/\text{Ni}^{2+}))$, $672\text{ cm}^{-1}(\text{T}_{2g}(\text{Cr}^{3+}))$ (Zhu et al., 2015). The evolution of the Raman spectra of a Cr-LMN electrode cycled at $C/24$ is shown in **Figure 3C** and has the following characteristics:

(1) Near the end of charge, the intensity of the 162 cm^{-1} band decreases and finally disappears, accompanied by the formation and growth of a new band at 170 cm^{-1} which is first observed at ~ 4.76 V ($x \sim 0.39$), and assigned to the translation mode of the lattice vibration, $\text{T}_{2g}(\text{T})$. This 4.76 V is close to the potential of the 2nd anodic peak in the plot of dQ/dV vs. V (Zhu et al., 2015) which is related to the oxidation of Ni^{3+} to Ni^{4+} . Compared to the phase diagram in **Figure 3E**, it is reasonable to assume that the appearance of the 170 cm^{-1} band corresponds to the presence of Phase-3 with less lithium. The lattice parameter of Phase-3 is $\sim 2\%$ smaller than that of Phase-1 leading to the up shift of this vibration mode from 162 to 170 cm^{-1} .

(2) A new band at $\sim 539\text{ cm}^{-1}$ is observed at the same time as the 170 cm^{-1} band and reaches its maximum as the voltage

approaches 4.9 V, it is identified as the symmetric vibration of the Ni^{4+} -O bond, $\text{T}_{2g}(\text{Ni}^{4+})$; simultaneously, the band at 528 cm^{-1} ($\text{T}_{2g}(\text{Ni}^{2+})$) fades away. The initial broadening of the 528 cm^{-1} band is attributed to the formation of the Ni^{3+} -O bond, and its disappearance indicates the $\text{Ni}^{2+}/\text{Ni}^{3+}$ are oxidized to Ni^{4+} .

(3) A small band is detected at $\sim 586\text{ cm}^{-1}$ as the voltage approaches 4.9 V and is attributed to the asymmetric vibration of the Ni^{4+} -O bond, which evolved from $\text{A}_{1g}(\text{Ni}^{2+}\text{-O})$ at 613 cm^{-1} .

(4) The broadening of the 498 cm^{-1} band is seen near 4.9 V, leading to the presence of a small new band at $\sim 486\text{ cm}^{-1}$ at ~ 4.9 V ($x \sim 0.12$), which is ascribed to a stretching mode of $\text{Ni}^{4+}\text{-O}$.

(5) During discharge, the evolution of the Raman bands proceeds reversely, all the new bands formed during charge fade away and the bands in the pristine cathode reappear.

In summary, the operando Raman spectroscopy study of Cr-LMN establishes the relation of oxidation state of Ni ion and the corresponding phases, i.e., Phase-2 is associated to the phase where all Ni^{2+} are converted to Ni^{3+} , i.e., $\text{Li}_{0.55}\text{Mn}_{1.45}\text{Ni}_{0.45}\text{Cr}_{0.1}\text{O}_4$. Similarly, $\text{Li}_{0.1}\text{Mn}_{1.45}\text{Ni}_{0.45}\text{Cr}_{0.1}\text{O}_4$ is Phase-3 at equilibrium, corresponds to the state where all of the nickel ions are converted to Ni^{4+} .

LiFePO₄

Lithium iron phosphate is one of the most investigated cathode material for lithium-ion batteries due to its high theoretical capacity (170 mAh/g), long cycle life, good thermal stability, high reversibility, low cost, non-toxicity and high safety characteristics (Joachin et al., 2009; Ramana et al., 2009; Dong et al., 2017). LiFePO_4 and FePO_4 (FP) have similar crystal structure described by space group $Pnma$, but different lattice parameters. When the LiFePO_4 cathode is charged and discharged, the Li^+ ions are de-intercalated and intercalated, respectively, along a channel in the $[010]$ direction (Islam et al., 2005; Li et al., 2018). Several models, such as Shrinking core model (Padhi et al., 1997), Domino cascade model (Delmas et al., 2008) describe the phase transformation between LiFePO_4 and FePO_4 , but the mechanism is still in debate. As a result, several operando techniques were applied to understand the process (Perea et al., 2012; Orikasa et al., 2013; Ouvrard et al., 2013; Dong et al., 2017), especially using operando XRD (Shin et al., 2008; Roberts et al., 2014) and operando Raman (Wu et al., 2013; Siddique et al., 2015). The $\text{LFP} \leftrightarrow \text{FP}$ transition is generally considered as a two-phase reaction (Chen et al., 2006; Laffont et al., 2006; Zhu Y. et al., 2013), also confirmed by XRD measurements conducted on slow cycled cells (Andersson et al., 2000; Shin et al., 2011; Siddique et al., 2015). **Figure 4A** shows the diffraction patterns (top) and corresponding cycling curve (bottom) at rate of $1C$. The transformation of LFP to FP was first observed at $\text{Li} = 0.62$ at $1C$, the same authors also reported the beginning of FP formation at $\text{Li} = 0.80$ at slower rate of $C/5$. The content of FP increases at the

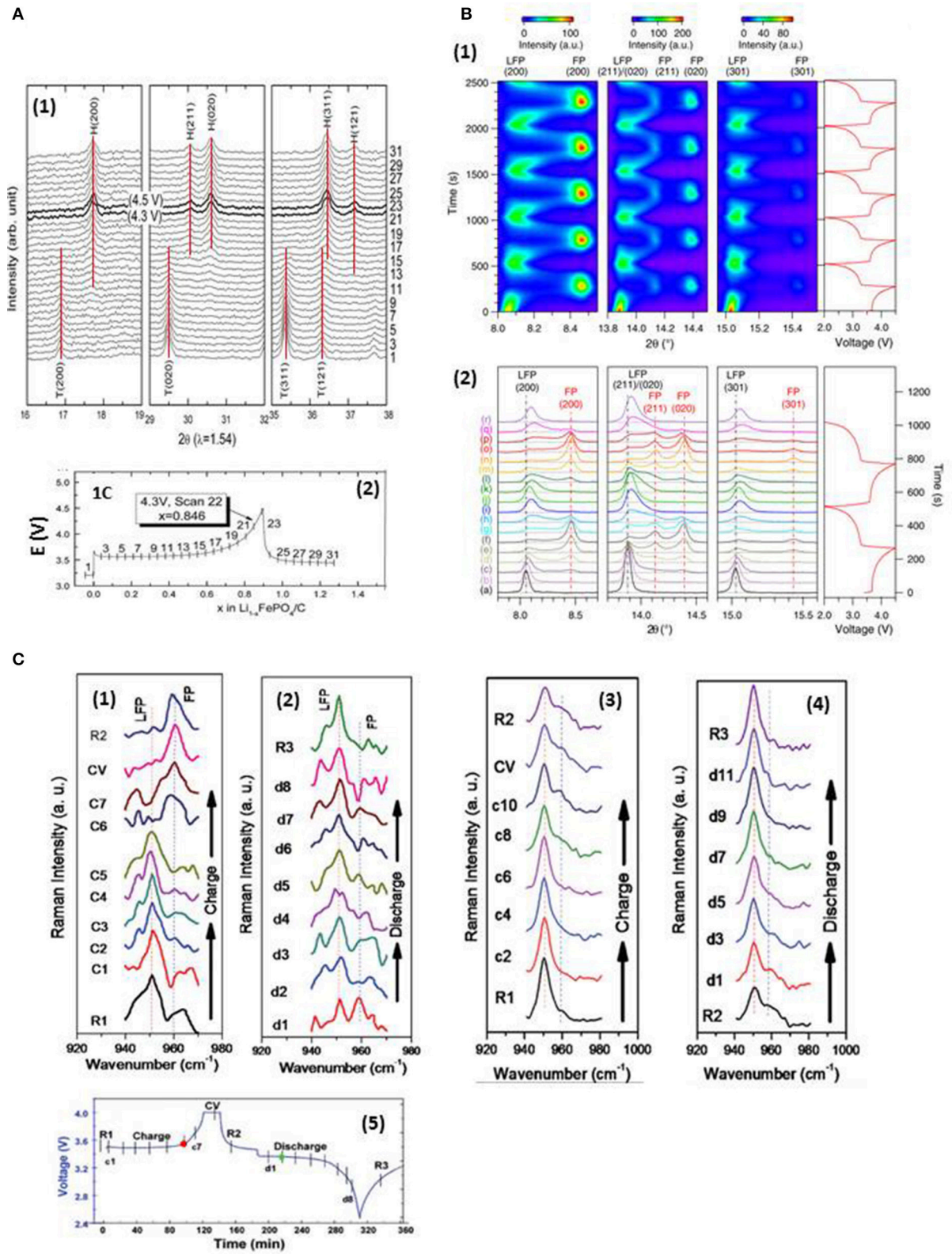


FIGURE 4 | (A) C-coated LiFePO_4 charged at 1C rate **(A1)** Evolution of XRD spectra shows that the FP is first detected at $\text{Li} = 0.62$, and the LFP disappears completely at 4.3V; **(A2)** corresponding charge-discharge curve (Shin et al., 2011 with permission from Elsevier); **(B)** LFP cycled at a rate of 10C (Liu, H. et al., 2014); **(B1)** image plot of diffraction patterns for (200), (211), (020), and (301) reflections during first five cycles; the scale bars of diffraction intensity are shown on top. *(Continued)*

FIGURE 4 | The corresponding voltage curve is plotted to the right. **(B2)** diffraction patterns from first two cycles stacked against the voltage profile; black vertical lines mark the positions of LFP peaks at the start of reaction; red vertical lines mark the position of FP peaks formed during the first cycle; with permission from AAAS. **(C)** Raman spectra collected on LFP electrode surface at a cycling rate of 0.3C (Siddique et al., 2015); **(C1)** carbon-rich spot A during charge; **(C2)** spot A during discharge; **(C3)** carbon-poor spot B during charge; **(C4)** spot B during discharge; **(C5)** corresponding electrochemical cell performance curve with vertical lines indicating the moment when the Raman spectra were taken; with permission from Wiley-VCH Verlag GmbH&Co. KGaA, Weinheim.

expense of LFP as charge proceeds, LFP disappeared completely after voltage reached 4.3 V; and the development of the phase reverses during discharge. The diffraction patterns show that the peak positions of the two phases are unchanged, suggesting a two phase reaction mechanism at the cycling rate of 1C or slower. The same technique is also used to explore the behavior of LFP nano-particles cycled at high rate. **Figure 4B** shows diffraction patterns (bottom) and the image plot of diffraction patterns (top) for (200), (211), (020), and (311) lines obtained on a LFP cathode cycled at 10C rate by using synchrotron X-ray ($\lambda = 0.7272\text{\AA}$). Authors indexed all the peaks observed to either the Li-rich $\text{Li}_{1-\alpha}\text{FePO}_4$ or the Li-poor $\text{Li}_\beta\text{FePO}_4$ in the space group Pnma. As expected in the cycling at slow rate, $\text{Li}_{1-\alpha}\text{FePO}_4$ peaks disappear on charge and are restored on discharge; $\text{Li}_\beta\text{FePO}_4$ peaks start to form and grow on charge and disappear on discharge. Unlike in the case of slow cycling, there are appreciable positive intensities within the 8.15° (LFP(200)) to 8.4° (FP(200)), 13.95° (LFP (211)/(020)) to 14.1° (FP(211)), and 15.15° (LFP(301)) to 15.4° (FP(301)) 2θ ranges, which indicate the existence of phases with lattice parameters that deviate from those of LiFePO_4 and FePO_4 under equilibrium (the corresponding (hkl) of LFP/FP are labeled in the parentheses). The phenomenon is more pronounced at 20C (not shown here). **Figure 4B2** shows that all the peaks are symmetrical at the onset of the first charge, the LFP(200) and (301) started to broaden asymmetrically toward higher angles as charge proceeded. The most severe asymmetrical broadening is around beginning of discharge in both 1st and 2nd cycles. Neither the peak position nor the peak shape of LFP is restored to that of the original state at the end of the discharge, indicating a solid solution of $\text{Li}_{1-\alpha}\text{FePO}_4$ was formed, which has smaller unit cell and more disordered structure compare to the pristine LFP. These results reveal a different mechanism at high cycling rate, i.e., LFP transforms to FP through a non-equilibrium solid solution instead of two-phase reaction. Capacity fading mechanism in a 18,650 commercial battery was also explored by in situ XRD; the authors observed a different mechanism in LFP/FP conversion after long cycling by formation of a single $\text{Li}_{1-x}\text{FePO}_4$ phase (Liu et al., 2018). These operando XRD investigations indicate that the working mechanism of the electrode materials may vary with the operating conditions, which may also shed the light on the failure mechanisms under different conditions.

The operando XRD examines the collective behavior of LFP particles on a centimeter scale, whereas Raman spectroscopy explores the local-phase transformation in the micrometer region. The conductivity of LFP is enhanced by adding carbon to the electrode. **Figure 4C** presents the Raman spectra collected from carbon-rich (**Figures 4C1,2**) and carbon-poor (**Figures 4C3,4**) regions of the electrodes during cycling at 0.3C. The bands at ~ 950 and 960 cm^{-1} are attributed to the symmetric stretching mode of PO_4^{3-} in LFP and FP. During

charge (**Figure 4C1**), the spectra show little change to the end of the 3.5 V plateau, then the 950 cm^{-1} band vanishes and 960 cm^{-1} band appears suddenly (red dot in **Figure 4C5**); the reverse change during discharge (**Figure 4C2**) is observed after the beginning of the discharge plateau (green dot in **Figure 4C5**). The evolution of the spectra demonstrates that the phase transformation between the LFP and FP particles is fast in the carbon-rich environment. A different phenomenon is seen in the carbon-poor area, where no abrupt phase change is detected during charge and discharge, (**Figures 4C3,4**); the main part of LFP does not participate in the reaction, which indicates that less carbon in the area reduces the local conductivity between the LFP particles, thus decreasing electrochemical charge transfer in the active material and leading to capacity loss. These results point out that the problem of capacity loss can be mitigated by converting the non-active regions of the electrode to active regions via homogenizing carbon distribution on a nano-scale. It is clear from both XRD and Raman that the progressive phase transformation observed via XRD is mainly attributed to the increase in the number of completely transformed particles.

Sulfur Cathode

Lithium-sulfur batteries have a high theoretical capacity of $1,675\text{ mAhg}^{-1}$ and utilize low-cost materials. The discharge mechanism of the sulfur electrode is a complex and controversial issue, which was investigated by various *in situ* techniques (Nelson et al., 2012; Cañas et al., 2013; Cui et al., 2013; Cuisinier et al., 2013; Hagen et al., 2013; Patel et al., 2013; Gorlin et al., 2015; Marceau et al., 2016; Paoletta et al., 2016). These studies indicate that elemental sulfur discharge is a multi-step process involving different intermediate species that are sensitive to the electrolyte and the operating conditions.

Operando XRD is used to study the battery working mechanism, but it cannot recognize the intermediate polysulfides (PSs) due to their non-crystalline nature. The phases which can be identified are the initial phase of $\alpha\text{-S}_8$ (orthorhombic, $a = 10.465$, $b = 12.866$, $c = 24.486$, S.G.: Fddd), the end product of discharge Li_2S ($a = 5.72\text{ \AA}$, S.G.: Fm $\bar{3}$ m), and end product of charge, $\beta\text{-S}_8$ (monoclinic, $a = 10.926$, $b = 10.855$, $c = 10.790\text{ \AA}$, $\beta = 95.92$, S.G.: P21/c) (Walus et al., 2013; Lowe et al., 2014), as shown in **Figure 5b** (Walus et al., 2013). To study this problem, fused silica is added to the electrolyte because it reacts with the intermediate species and leads to specific absorption of long chain poly-sulfides to form an organized layer (Lay et al., 2003; Hwang et al., 2016) from which the finger prints of the absorbed poly-sulfides are detected via XRD. **Figure 5a** (Conder et al., 2017) shows the evolution of the XRD spectra from the cell with fused silica during the first cycle (left), the corresponding contour plot (right), and the galvanostatic curve (center). The starting red pattern is from

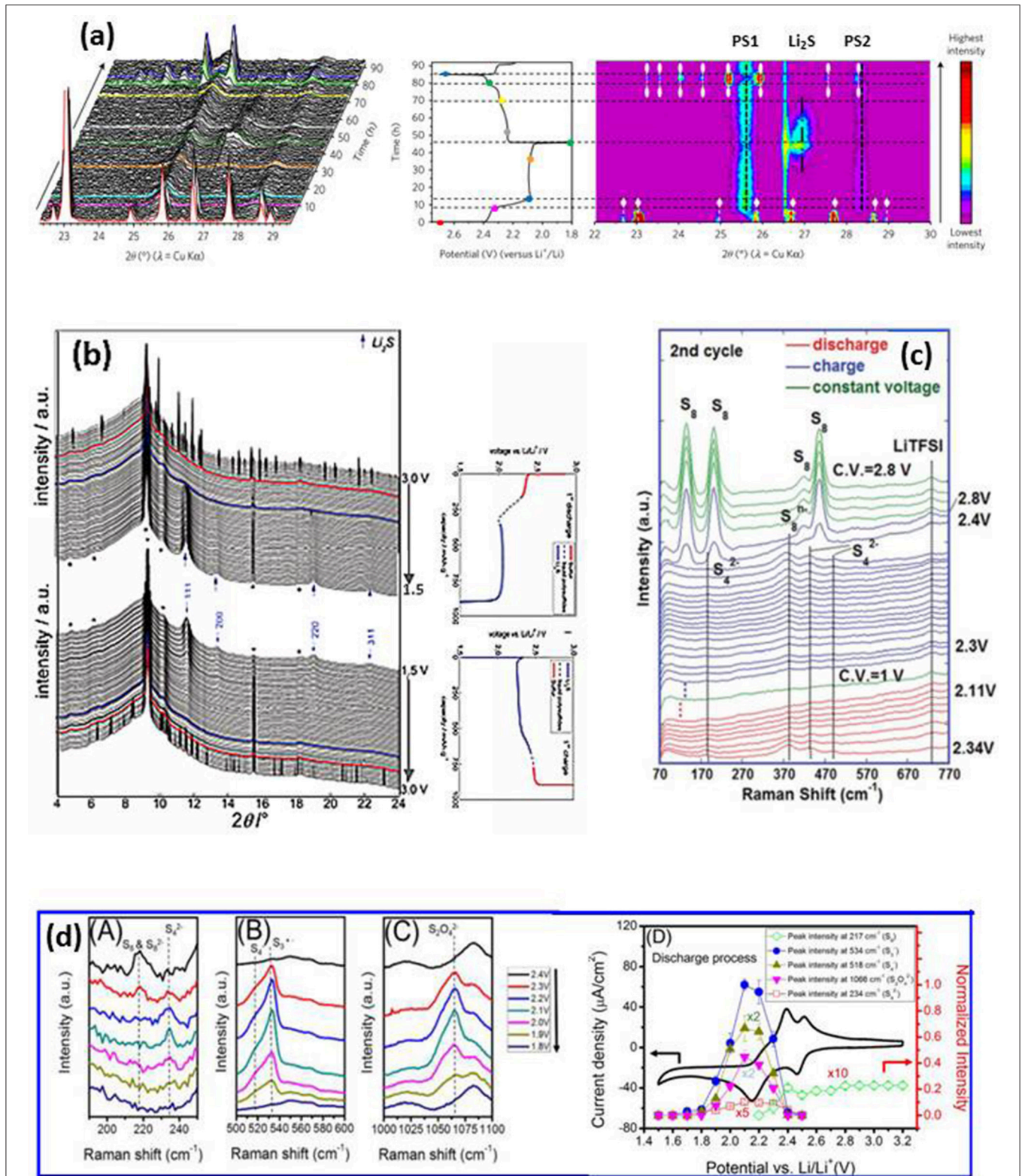


FIGURE 5 | (a) Development of XRD patterns of a Li-S cell with fused silica additive during first cycle (left), corresponding galvanostatic curve at C/50 (center) and XRD image plot (right). The colored patterns (left) correspond to colored dots on the cycling curve (center). α -S₈ and β -S₈ are represented by white lines with diamond and oval symbols, respectively (right). PS1 and PS2 are attributed to the PS-SiO₂ interactions (vertical black dashed lines). Li₂S is symbolized by a dashed-dotted black vertical line; * is from cell package (Conder et al., 2017); with permission from Springer Nature; (b) XRD patterns of a cell during 1st cycle with corresponding (Continued)

FIGURE 5 | electrochemical plot; arrow, Li_2S ; *, cell package; bold lines indicate initial appearance of solid phase and subsequent disappearance (Walus et al., 2013); with permission from RSC; **(c)** Raman spectra from 1 M LiTFSI-DOL-DME electrolyte on the lithium side during first cycle; * separator (Zhu et al., 2017). **(dA-C)** Raman spectra of sulfur cathode during discharge; **(dD)** Cyclic voltammetry of as-prepared sulfur-carbon cathode and potential dependence of the peak intensities (Wu et al., 2015); with permission from ACS.

$\alpha\text{-S}_8$. It disappears quickly as discharge begins, and two broad peaks are observed at 25.56° and 28.32° immediately (labeled PS1 and PS2 respectively). At this early stage of lithiation, the peaks may be related only to the long-chain PSs, the authors attributed them to Li_2S_8 , or to Li_2S_6 . These two peaks reach a maximum at the end of the first discharge plateau on which the lithiation corresponds to a liquid-liquid equilibrium and Li_2S_8 is reduced to Li_2S_6 , then to Li_2S_4 . Near the end of discharge, a new peak at $\sim 27^\circ$ is detected (orange pattern) that is ascribed to cubic Li_2S . Meanwhile PS1 and PS2 decrease toward the end of the discharge, but do not disappear completely, indicating the incomplete reduction of PS1/PS2. During charge, the phase evolution process is reversed, except the final product is monoclinic $\beta\text{-S}_8$ (green) instead of $\alpha\text{-S}_8$.

The nature of the non-crystalline intermediate PSs formed during cycling makes the XRD analysis difficult, even with the above-mentioned method. On the other hand, Raman spectroscopy can clearly detect different species formed in the cathode and dissolved in the electrolyte (Yeon et al., 2012; Hannauer et al., 2015; Paoletta et al., 2018). **Figure 5c** (Zhu et al., 2017) displays the development of Raman spectra of the electrolyte (1M LiTFSI-DME-DOL) near the lithium anode during the 2nd cycle. It is interesting to note that elemental sulfur is observed at the end of charge near lithium anode; this sulfur is $\beta\text{-S}_8$ according to operando XRD, which cannot be distinguished from $\alpha\text{-S}_8$ by Raman spectra in the measured region. The loss of active material near the lithium anode reduces the local conductivity and corrodes the lithium, which has a negative effect on battery capacity and cycle life. The effect of the electrolyte on the discharge mechanism was also studied in the same work. The species detected in the 1M LiTFSI-DME-DOL electrolyte near the Li electrode of an as made cell are S_8^{n-} and S_4^{2-} , indicating a rapid self-discharge in this widely used liquid electrolyte. In contrast, self-discharge is much slower in an ionic liquid, where elemental S_8 began to appear on the lithium side at the middle of the high-voltage plateau, and remains until the end of the plateau where S_8^{n-} and S_4^{2-} are observed. The mechanism and kinetics of sulfur reduction in LiTFSI-TEGDME-DIOX electrolyte was investigated by operando Raman, and the results are shown in **Figure 5d** (Wu et al., 2015). $\text{S}_8/\text{S}_8^{2-}$, S_4^{2-} , S_4^- and S_3^{1-} are detected at different stages of discharge, and the process is summarized as (1) the formation of long chain PSs as S_8 ring opens at $\sim 2.4\text{V}$; (2) the short chain PSs start to form at $\sim 2.3\text{V}$ and they decompose again at 1.6V . The rate constants of different species are obtained from the evolution of the spectra by fitting the appearance and disappearance of bands to a pseudo first order reaction. Compared to the PSs observed in LiTFSI-DME-DOL, an additional specie S_3^{1-} is detected in LiTFSI-TEGDME-DIOX, indicating that the intermediate PSs are sensitive to the electrolyte used, thus the different

discharge mechanisms may vary with the electrolyte chosen. The insights gained from operando Raman analysis provide an explanation for one of the causes of capacity fade, and may be a helpful guide in the selection of a more appropriate electrolyte.

CONCLUSIONS

We reviewed the application of operando X-ray diffraction and operando Raman techniques to characterize operating batteries along with the importance of these techniques to help researchers to understand how the rechargeable batteries work, why they behave in their specific ways, how and why they fail. Operando XRD provides information on the average crystal structural changes of electrodes during cycling. Operando Raman probes the structure of individual particle on the electrode surface, the electrode-electrolyte interface and the electrolyte as well as the species in it to reveal information related to the oxidation state of ions and the interatomic bond length, etc. Raman maps constructed from the information collected describe the behavior of individual electrode particles under operating condition and their influence on the kinetics of phase transformation that is directly related to the battery rate capacity and cycle life. The information obtained by both in situ XRD and Raman methods leads to an atomic level understanding of the variations of structure and its stability, the development of surface and interface structures, which are critical to the battery performance. But for the improvement of the existing electrode materials, the design of new high performance materials, we need more advanced in-situ techniques to reveal the working and degradation mechanisms of different materials. For this purpose, the present operando techniques have to be ameliorated and developed in the directions of (1) multi-functioning, to allow collecting different types of information simultaneously; (2) capability of obtaining 3D morphology information of electrode which is important for improving electrode quality; (3) rapid measurement/fast data collection, to monitor the non-equilibrium state and the rate effect on the materials; (4) ability of measuring the desired materials in the same environment and conditions as the battery in practical applications.

AUTHOR CONTRIBUTIONS

WZ wrote the draft. All authors contributed to the writing, discussion and revision of the final version.

FUNDING

Centre d'excellence en électrification des transports et stockage d'énergie, Québec, Canada.

REFERENCES

- Amatucci, G. G., Tarascon, J. M., and Klein, C. (1996). CoO₂ the end member of the LiCoO₂ solid solution. *J. Electrochem. Soc.* 143, 1114–1123. doi: 10.1149/1.1836594
- Amdouni, N., Zaghib, K., Gendron, F., Mauger, A., and Julien, C. M. (2006). Structure and insertion properties of disordered and ordered LiNi_{0.5}Mn_{1.5}O₄ spinels prepared by wet chemistry. *Ionics (Kiel)* 12, 117–126. doi: 10.1007/s11581-006-0021-7
- Amine, K., Tukamoto, H., Yasuda, H., and Fuiita, Y. (1996). A new three-volt spinel Li₁+Mn_{1.5}Ni_{0.5}O₄ for secondary lithium batteries. *J. Electrochem. Soc.* 143, 1607–1613. doi: 10.1149/1.1836686
- Andersson, A. S., Kalska, B., Häggström, L., and Thomas, J. O. (2000). Lithium extraction/insertion in LiFePO₄: an X-ray diffraction and Mössbauer spectroscopy study. *Solid State Ionics* 130, 41–52. doi: 10.1016/S0167-2738(00)00311-8
- Armand, M., and Tarascon, J.-M. (2008). Building better batteries. *Nature* 451, 652–657. doi: 10.1038/451652a
- Aurbach, D., and Chusid, O. (1997). The use of in situ Fourier-transform infrared spectroscopy for the study of surface phenomena on electrodes in selected lithium battery electrolyte solutions. *J. Power Sour.* 68, 463–470. doi: 10.1016/S0378-7753(97)02622-0
- Baddour-Hadjean, R., and Pereira-Ramos, J.-P. (2010). Raman microspectrometry applied to the study of electrode materials for lithium batteries. *Chem. Rev.* 110, 1278–1319. doi: 10.1021/cr800344k
- Berckmans, G., Messagie, M., Smekens, J., Omar, N., Vanhaverbeke, L., and Mierlo, J. V. (2017). Cost Projection of state of the art lithium-ion batteries for electric vehicles up to 2030. *Energies* 10:1314. doi: 10.3390/en10091314
- Bleith, P., Kaiser, H., Novák, P., and Villeville, C. (2015). In situ X-ray diffraction characterisation of Fe_{0.5}TiOPO₄ and Cu_{0.5}TiOPO₄ as electrode material for sodium-ion batteries. *Electrochim. Acta* 176, 18–21. doi: 10.1016/j.electacta.2015.06.105
- Bobrikov, I. A., Balagurov, A. M., Hu, C.-W., Lee, C.-H., Chen, T.-Y., Deleg, S., et al. (2014). Structural evolution in LiFePO₄-based battery materials: in-situ and ex-situ time-of-flight neutron diffraction study. *J. Power Sour.* 258, 356–364. doi: 10.1016/j.jpowsour.2014.02.060
- Bobrikov, I. A., Samoylova, N. Y., Sumnikov, S. V., Ivanshina, O. Y., Vasin, R. N., Beskrovnyi, A. I., et al. (2017). In-situ time-of-flight neutron diffraction study of the structure evolution of electrode materials in a commercial battery with LiNi_{0.8}Co_{0.15}Al_{0.05}O₂ cathode. *J. Power Sour.* 372, 74–81. doi: 10.1016/j.jpowsour.2017.10.052
- Budde-Meiwes, H., Drillkens, J., Lunz, B., Muennix, J., Rothgang, S., Kowal, J., et al. (2013). A review of current automotive battery technology and future prospects. *Proc. Inst. Mech. Eng. Part D J. Automob. Eng.* 227, 761–776. doi: 10.1177/0954407013485567
- Cañas, N. A., Einsiedel, P., Freitag, O. T., Heim, C., Steinhauer, M., Park, D.-W., et al. (2017). Operando X-ray diffraction during battery cycling at elevated temperatures: a quantitative analysis of lithium-graphite intercalation compounds. *Carbon* 116, 255–263. doi: 10.1016/j.carbon.2017.02.002
- Cañas, N. A., Wolf, S., Wagner, N., and Friedrich, K. A. (2013). In-situ X-ray diffraction studies of lithium-sulfur batteries. *J. Power Sour.* 226, 313–319. doi: 10.1016/j.jpowsour.2012.10.092
- Carter, R., Huhman, B., Love, C. T., and Zenyuk, I. V. (2018). X-ray computed tomography comparison of individual and parallel assembled commercial lithium iron phosphate batteries at end of life after high rate cycling. *J. Power Sour.* 381, 46–55. doi: 10.1016/j.jpowsour.2018.01.087
- Chan, H.-W., Duh, J.-G., and Lee, J.-F. (2006). Valence change by in situ XAS in surface modified LiMn₂O₄ for Li-ion battery. *Electrochem. Commun.* 8, 1731–1736. doi: 10.1016/j.elecom.2006.07.038
- Chen, G., Song, X., and Richardson, T. J. (2006). Electron microscopy study of the LiFePO₄ to FePO₄ phase transition. *Electrochem. Solid State Lett.* 9, A295–A298. doi: 10.1149/1.2192695
- Chen, K., Cao, K., Xing, C., Hu, Y., Liu, J., He, Y., et al. (2016a). In-situ TEM study of the lithiation and delithiation of FeS nanosheets. *J. Alloys Comp.* 688, 946–952. doi: 10.1016/j.jallcom.2016.07.008
- Chen, Z., and Dahn, J. R. (2004). Methods to obtain excellent capacity retention in LiCoO₂ cycled to 4.5 V. *Electrochim. Acta* 49, 1079–1090. doi: 10.1016/j.electacta.2003.10.019
- Chen, Z., Lu, Z., and Dahn, J. R. (2002). Staging phase transitions in Li[_x]CoO[_{sub 2}]. *J. Electrochem. Soc.* 149, A1604–A1609. doi: 10.1149/1.1519850
- Chen, Z., Wang, J., Chao, D., Baikie, T., Bai, L., Chen, S., et al. and Shen, Z. (2016b). Hierarchical porous LiNi_{1/3}Co_{1/3}Mn_{1/3}O₂ Nano-/micro spherical cathode material: minimized cation mixing and improved Li⁺ mobility for enhanced electrochemical performance. *Sci. Rep.* 6:25771. doi: 10.1038/srep25771
- Cheng, H., Zhu, C. B., Lu, M., and Yang, Y. (2007). In situ micro-FTIR study of the solid–solid interface between lithium electrode and polymer electrolytes. *J. Power Sour.* 174, 1027–1031. doi: 10.1016/j.jpowsour.2007.06.213
- Chung, K. Y., Yoon, W.-S., Lee, H. S., McBreen, J., Yang, X.-Q., Oh, S. H., et al. (2006). In situ XRD studies of the structural changes of ZrO₂-coated LiCoO₂ during cycling and their effects on capacity retention in lithium batteries. *J. Power Sour.* 163, 185–190. doi: 10.1016/j.jpowsour.2005.12.063
- Chung, K. Y., Yoon, W.-S., McBreen, J., Yang, X. Q., Oh, S. Y., Shim, H. C., et al. (2007). In situ X-ray diffraction studies on the mechanism of capacity retention improvement by coating at the surface of LiCoO₂. *J. Power Sour.* 174, 619–623. doi: 10.1016/j.jpowsour.2007.06.242
- Chusid, O., Gofer, Y., Aurbach, D., Watanabe, M., Momma, T., and Osaka, T. (2001). Studies of the interface between lithium electrodes and polymeric electrolyte systems using in situ FTIR spectroscopy. *J. Power Sour.* 97–98, 632–636. doi: 10.1016/S0378-7753(01)00643-7
- Conder, J., Bouchet, R., Trabesinger, S., Marino, C., Gubler, L., and Villeville, C. (2017). Direct observation of lithium polysulfides in lithium-sulfur batteries using operando X-ray diffraction. *Nat. Energy* 2:17069. doi: 10.1038/nenergy.2017.69
- Cui, Y., Abouimrane, A., Lu, J., Bolin, T., Ren, Y., Weng, W., et al. (2013). (De)Lithiation Mechanism of Li/Se_x (x = 0–7) batteries determined by in situ synchrotron X-ray diffraction and X-ray absorption spectroscopy. *J. Am. Chem. Soc.* 135, 8047–8056. doi: 10.1021/ja402597g
- Cuisinier, M., Cabelguen, P.-E., Evers, S., He, G., Kolbeck, M., Garsuch, A., et al. (2013). Sulfur speciation in Li-S batteries determined by operando X-ray absorption spectroscopy. *J. Phys. Chem. Lett.* 4, 3227–3232. doi: 10.1021/jz401763d
- Delmas, C., Maccario, M., Croguennec, L., Le Cras, F., and Weill, F. (2008). Lithium deintercalation in LiFePO₄ nanoparticles via a domino-cascade model. *Nat. Mater.* 7, 665–671. doi: 10.1038/nmat2230
- Dokko, K., Anzue, N., Mohamedi, M., Itoh, T., and Uchida, I. (2004). Raman spectro-electrochemistry of LiCo_xMn_{2-x}O₄ thin film electrodes for 5 V lithium batteries. *Electrochem. Commun.* 6, 384–388. doi: 10.1016/j.elecom.2004.02.005
- Dokko, K., Mohamedi, M., Anzue, N., Itoh, T., and Uchida, I. (2002). In situ Raman spectroscopic studies of LiNi_xMn_{2-x}O₄ thin film cathode materials for lithium ion secondary batteries. *J. Mater. Chem.* 12, 3688–3693. doi: 10.1039/B206764A
- Dolotko, O., Senyshyn, A., Mühlbauer, M. J., Nikolowski, K., and Ehrenberg, H. (2014). Understanding structural changes in NMC Li-ion cells by in situ neutron diffraction. *J. Power Sour.* 255, 197–203. doi: 10.1016/j.jpowsour.2014.01.010
- Dominko, R., Arçon, I., Kodre, A., Hanžel, D., and Gaberšček, M. (2009). In-situ XAS study on Li₂MnSiO₄ and Li₂FeSiO₄ cathode materials. *J. Power Sour.* 189, 51–58. doi: 10.1016/j.jpowsour.2008.11.077
- Dong, H., Guo, H., He, Y., Chen, D., Li, H., Gao, J., et al. (2017). Structural stability and Li-ion transport property of LiFePO₄ under high-pressure. *Solid State Ionics* 301, 133–137. doi: 10.1016/j.ssi.2017.01.026
- Dunn, B., Kamath, H., and Tarascon, J.-M. (2011). Electrical energy storage for the grid: a battery of choices. *Science* 334, 928–935. doi: 10.1126/science.1212741
- Etacheri, V., Marom, R., Elazari, R., Salitra, G., and Aurbach, D. (2011). Challenges in the development of advanced Li-ion batteries: a review. *Energy Environ. Sci.* 4, 3243–3262. doi: 10.1039/C1EE01598B
- Fehse, M., Monconduit, L., Fischer, F., Tessier, C., and Stievano, L. (2014). Study of the insertion mechanism of lithium into anatase by operando X-ray diffraction and absorption spectroscopy. *Solid State Ionics* 268, 252–255. doi: 10.1016/j.ssi.2014.09.018
- Giorgetti, M. (2013). A review on the structural studies of batteries and host materials by X-Ray absorption spectroscopy. *ISRN Mater. Sci.* 2013, 1–22. doi: 10.1155/2013/938625
- Girishkumar, G., McCloskey, B., Luntz, A. C., Swanson, S., and Wilcke, W. (2010). Lithium-Air battery: promise and challenges. *J. Phys. Chem. Lett.* 1, 2193–2203. doi: 10.1021/jz1005384

- Giuliana, A., Marco, G., Robert, D., Lorenzo, S., Iztok, A., Nicola, N., et al. (2017). Operando characterization of batteries using x-ray absorption spectroscopy: advances at the beamline XAFS at synchrotron elettrra. *J. Phys. D Appl. Phys.* 50:074001. doi: 10.1088/1361-6463/aa519a
- Godbole, V. A., Colin, J.-F., and Nováka, A. P. (2011). Study of Overcharge behavior of $\text{Li}_{1-x}(\text{Ni}_{1/3}\text{Mn}_{1/3}\text{Co}_{1/3})_1\text{-xO}_2$ using in situ and ex situ X-ray synchrotron diffraction. *J. Electrochem. Soc.* 158, A1005–A1010. doi: 10.1149/1.3607982
- Goodenough, J. B., and Kim, Y. (2010). Challenges for rechargeable Li Batteries. *Chem. Mater.* 22, 587–603. doi: 10.1021/cm901452z
- Gorlin, Y., Siebel, A., Piana, M., Huthwelker, T., Jha, H., Monsch, G., et al. (2015). Operando Characterization of Intermediates produced in a Lithium-Sulfur Battery. *J. Electrochem. Soc.* 162, A1146–A1155. doi: 10.1149/2.0081507jes
- Gross, T., and Hess, C. (2014). Raman diagnostics of LiCoO_2 electrodes for lithium-ion batteries. *J. Power Sour.* 256, 220–225. doi: 10.1016/j.jpowsour.2014.01.084
- Hagen, M., Schiffels, P., Hammer, M., Dorfler, S., Tubke, J., Hoffmann, M. J., et al. (2013). In-Situ raman investigation of polysulfide formation in Li-S cells. *J. Electrochem. Soc.* 160, A1205–A1214. doi: 10.1149/2.045308jes
- Hannauer, J., Scheers, J., Fullenwarth, J., Fraise, B., Stievano, L., and Johansson, P. (2015). The quest for polysulfides in Lithium-Sulfur battery electrolytes: an operando confocal raman spectroscopy study. *Chemphyschem* 16, 2755–2759. doi: 10.1002/cphc.201500448
- Hardwick, L. J., Ruch, P. W., Hahn, M., Scheifele, W., Kötz, R., and Novák, P. (2008). In situ raman spectroscopy of insertion electrodes for lithium-ion batteries and supercapacitors: first cycle effects. *J. Phys. Chem. Solids* 69, 1232–1237. doi: 10.1016/j.jpccs.2007.10.017
- Harks, P. P. R. M. L., Mulder, F. M., and Notten, P. H. L. (2015). In situ methods for Li-ion battery research: a review of recent developments. *J. Power Sour.* 288, 92–105. doi: 10.1016/j.jpowsour.2015.04.084
- He, H., Huang, C., Luo, C.-W., Liu, J.-J., and Chao, Z.-S. (2013). Dynamic study of Li intercalation into graphite by in situ high energy synchrotron XRD. *Electrochim. Acta* 92, 148–152. doi: 10.1016/j.electacta.2012.12.135
- Hovington, P., Dontigny, M., Guerfi, A., Trottier, J., Lagacé, M., Mauger, A., et al. (2014). In situ Scanning electron microscope study and microstructural evolution of nano silicon anode for high energy Li-ion batteries. *J. Power Sour.* 248, 457–464. doi: 10.1016/j.jpowsour.2013.09.069
- Hu, S.-K., Cheng, G.-H., Cheng, M.-Y., Hwang, B.-J., and Santhanam, R. (2009). Cycle life improvement of ZrO_2 -coated spherical $\text{LiNi}_{1/3}\text{Co}_{1/3}\text{Mn}_{1/3}\text{O}_2$ cathode material for lithium ion batteries. *J. Power Sour.* 188, 564–569. doi: 10.1016/j.jpowsour.2008.11.113
- Huang, Z. D., Liu, X. M., Oh, S. W., Zhang, B., Maa, P. C., and Kim, J. K. (2011). Microscopically porous, interconnected single crystal $\text{LiNi}_{1/3}\text{Co}_{1/3}\text{Mn}_{1/3}\text{O}_2$ cathode material for Lithium ion batteries. *J. Mater. Chem.* 21, 10777–10784. doi: 10.1039/C1JM00059D
- Hugues, D., Hai, B., Leskes, M., Grey, C. P., and Chen, G. (2014). Relationships between Mn^{3+} content, structural ordering, phase transformation, and kinetic properties in $\text{LiNi}_x\text{Mn}_{2-x}\text{O}_4$ cathode materials. *Chem. Mater.* 26, 5374–5382. doi: 10.1021/cm502607v
- Hwang, B. J., Tsai, Y. W., Carlier, D., and Ceder, G. (2003). A combined computational/experimental study on $\text{LiNi}_{1/3}\text{Co}_{1/3}\text{Mn}_{1/3}\text{O}_2$. *Chem. Mater.* 15, 3676–3682. doi: 10.1021/cm030299v
- Hwang, J. Y., Kim, C. M., Lee, S. K., Lee, J. H., Abouimrane, A., Mo Khaleel, M. A., et al. (2016). Lithium-Sulfur batteries: high-energy, high-rate, lithium-sulfur batteries: synergetic effect of hollow TiO_2 -webbed carbon nanotubes and a dual functional carbon-paper interlayer. *Adv. Energy Mater.* 6:1501480 doi: 10.1002/aenm.201501480
- Inaba, M., Iriyama, Y., Ogumi, Z., Todzuka, Y., and Tasaka, A. (1997). Raman study of layered rock-salt LiCoO_2 and its electrochemical lithium deintercalation. *J. Raman Spectrosc.* 28, 613–617. doi: 10.1002/(SICI)1097-4555(199708)28:8<613::AID-JRS138>3.0.CO;2-T
- Islam, M. S., Driscoll, D. J., Fisher, C. A. J., and Slater, P. R. (2005). Atomic-scale investigation of defects, dopants, and lithium transport in the LiFePO_4 olivine-type battery material. *Chem. Mater.* 17, 5085–5092. doi: 10.1021/cm050999v
- Itoh, T., Sato, H., Nishina, T., Matue, T., and Uchida, I. (1997). In situ Raman spectroscopic study of LiCoO_2 electrodes in propylene carbonate solvent systems. *J. Power Sour.* 68, 333–337. doi: 10.1016/S0378-7753(97)02539-1
- Janish, M. T., and Carter, C. B. (2015). In situ TEM observations of the lithiation of molybdenum disulfide. *Scr. Mater.* 107, 22–25. doi: 10.1016/j.scriptamat.2015.05.011
- Ji, X., and Nazar, L. F. (2010). Advances in Li-S batteries. *J. Mater. Chem.* 20, 9821–9826. doi: 10.1039/b925751a
- Joachim, H., Kaun, T. D., Zaghbi, K., and Prakasha, J. (2009). electrochemical and thermal studies of carbon-coated LiFePO_4 cathode. *J. Electrochem. Soc.* 156, A401–A406. doi: 10.1149/1.3106121
- Julien, C. M., Mauger, A., Zaghbi, K., and Groult, H. (2014). Comparative issues of cathode materials for Li-Ion batteries. *Inorganics* 2, 132–154. doi: 10.3390/inorganics2010132
- Kim, J.-H., Myung, S.-T., Yoon, C. S., Kang, S. G., and Sun, Y.-K. (2004). Comparative study of $\text{LiNi}_0.5\text{Mn}_1.5\text{O}_4$ - δ and $\text{LiNi}_0.5\text{Mn}_1.5\text{O}_4$ cathodes having two crystallographic structures: $\text{Fd}3\text{hm}$ and P4332 . *Chem. Mater.* 16, 906–914. doi: 10.1021/cm035050s
- Komatsu, H., Arai, H., Koyama, Y., Sato, K., Kato, T., Yoshida, R., et al. (2015). Solid solution domains at phase transition front of $\text{Li}_x\text{Ni}_0.5\text{Mn}_1.5\text{O}_4$. *Adv. Energy Mater.* 5:1500638. doi: 10.1002/aenm.201500638
- Kostecki, R., and McLarnon, F. (2004). Local-Probe studies of degradation of composite $\text{LiNi}_0.8\text{Co}_0.15\text{Al}_0.05\text{O}_2$ cathodes in high-power lithium-ion cells. *Electrochem. Solid-State Lett.* 7, A380–A383. doi: 10.1149/1.1793771
- Kraatzberg, A., and Ein-Eli, Y. (2011). Review on Li-air batteries—opportunities, limitations and perspective. *J. Power Sour.* 196, 886–893. doi: 10.1016/j.jpowsour.2010.09.031
- Kunduraci, M., Al-Sharab, J. F., and Amatucci, G. G. (2006). High-Power nanostructured $\text{LiMn}_{2-x}\text{Ni}_x\text{O}_4$ high-voltage lithium-ion battery electrode materials: electrochemical impact of electronic conductivity and morphology. *Chem. Mater.* 18, 3585–3592. doi: 10.1021/cm060729s
- Kunduraci, M., and Amatucci, G. G. (2006). Synthesis and characterization of nanostructured 4.7 V $\text{Li}_{[x]}\text{Mn}_{[1.5]}\text{Ni}_{[0.5]}\text{O}_{[4]}$ spinels for high-power lithium-ion batteries. *J. Electrochem. Soc.* 153, A1345–A1352. doi: 10.1149/1.2198110
- Laffont, L., Delacourt, C., Gibot, P., Wu, M. Y., Kooyman, P., Masquelier, C., et al. (2006). Study of the $\text{LiFePO}_4/\text{FePO}_4$ two-phase system by high-resolution electron energy loss spectroscopy. *Chem. Mater.* 18, 5520–5529. doi: 10.1021/cm0617182
- Lay, M. D., Varazo, K., and Stickney, J. L. (2003). Formation of sulfur atomic layers on gold from aqueous solutions of sulfide and thiosulfate: studies using ECSTM, UHV-EC, and TLEC. *Langmuir* 19, 8416–8427. doi: 10.1021/la034474y
- Leriche, J. B., Hamelet, S., Shu, J., Morcrette, M., Masquelier, C., Ouvrard, G., et al. (2010). An electrochemical cell for operando study of lithium batteries using synchrotron radiation. *J. Electrochem. Soc.* 157, A606–A610. doi: 10.1149/1.3355977
- Li, J., Petibon, R., Glazier, S., Sharma, N., Pang, W. K., Peterson, V. K., et al. (2015). In-situ neutron diffraction study of a high voltage $\text{Li}(\text{Ni}_0.42\text{Mn}_0.42\text{Co}_0.16)\text{O}_2/\text{graphite}$ pouch cell. *Electrochim. Acta* 180, 234–240. doi: 10.1016/j.electacta.2015.08.122
- Li, W., Reimers, J. N., and Dahn, J. R. (1993). In situ X-ray diffraction and electrochemical studies of $\text{Li}_x\text{-NiO}_2$. *Solid State Ionics* 67, 123–130. doi: 10.1016/0167-2738(93)90317-V
- Li, Z., Yang, J., Li, C., Wang, S., Zhang, L., Zhu, K., et al. (2018). Orientation-dependent lithium miscibility gap in LiFePO_4 . *Chem. Mater.* 30, 874–878. doi: 10.1021/acs.chemmater.7b04463
- Liao, X., Sun, P., Xu, M., Xing, L., Liao, Y., Zhang, Y., et al. (2016). Application of tris(trimethylsilyl)borate to suppress self-discharge of layered nickel cobalt manganese oxide for high energy battery. *Appl. Energy* 175, 505–511. doi: 10.1016/j.apenergy.2016.03.114
- Liu, H., Strohbridge, F. C., Borkiewicz, O. J., Wiaderek, K. M., Chapman, K. W., Chupas, P. J., et al. (2014). Capturing metastable structures during high-rate cycling of LiFePO_4 nanoparticle electrodes. *Science* 344:1252817. doi: 10.1126/science.1252817
- Liu, Q., Liu, Y., Yang, F., He, H., Xiao, X., Ren, Y., et al. (2018). Capacity fading mechanism of the commercial 18650 LiFePO_4 -based lithium-ion batteries: an in situ time-resolved high-energy synchrotron XRD study. *ACS Appl. Mater. Interfaces* 10, 4622–4629. doi: 10.1021/acsami.7b13060
- Liu, S., Xie, J., Su, Q., Du, G., Zhang, S., Cao, G., et al. (2014). Understanding Li-storage mechanism and performance of MnFe_2O_4 by in situ TEM observation

- on its electrochemical process in nano lithium battery. *Nano Energy* 8, 84–94. doi: 10.1016/j.nanoen.2014.06.001
- Lowe, M. A., Gao, J., and Abruña, H. D. (2014). Mechanistic insights into operational lithium–sulfur batteries by in situ X-ray diffraction and absorption spectroscopy. *RSC Adv.* 4:18347. doi: 10.1039/c4ra01388c
- Lu, Z., and Dahn, J. R. (2002). Understanding the anomalous capacity of Li/Li[Ni_xLi_{1-x}](1/3–2x/3)[Mn_{2/3-x/3}][O₂] cells using *In Situ* X-Ray diffraction and electrochemical studies. *J. Electrochem. Soc.* 149, A815–A822. doi: 10.1149/1.1480014
- Ma, R., Shao, L., Wu, K., Shui, M., Wang, D., Pan, J., et al. (2013). Comparison of LiVPO₄F to Li₄Ti₅O₁₂ as anode materials for lithium-ion batteries. *ACS Appl. Mater. Interfaces* 5, 8615–8627. doi: 10.1021/am402132u
- MacNeil, D. D., Lu, Z., Chen, Z., and Dahn, J. R. (2002). A comparison of the electrode/electrolyte reaction at elevated temperatures for various Li-ion battery cathodes. *J. Power Sour.* 108, 8–14. doi: 10.1016/S0378-7753(01)01013-8
- Manthiram, A., Fu, Y., and Su, A. S. (2013). Challenges and prospects of lithium-sulfur batteries. *Acc. Chem. Res.* 46, 1125–1134. doi: 10.1021/ar300179v
- Marceau, H., Kim, C.-S., Paoella, A., Ladouceur, S., Lagacé, M., Chaker, M., et al. (2016). In operando scanning electron microscopy and ultraviolet-visible spectroscopy studies of lithium/sulfur cells using all solid-state polymer electrolyte. *J. Power Sour.* 319, 247–254. doi: 10.1016/j.jpowsour.2016.03.093
- Membreno, N., Xiao, P., Park, K. S., Goodenough, J. B., Henkelman, G., and Stevenso, K. J. (2013). *In Situ* raman study of phase stability of α -Li₃V₂(PO₄)₃ upon thermal and laser heating. *J. Phys. Chem. C* 117, 11994–12002. doi: 10.1021/jp403282a
- Menzel, M., Schlifke, A., Falk, M., Janek, J., Fröba, M., and Fittschen, U. E. A. (2013). Surface and in-depth characterization of lithium-ion battery cathodes at different cycle states using confocal micro-X-ray fluorescence-X-ray absorption near edge structure analysis. *Spectrochim. Acta Part B Atomic Spectrosc.* 85, 62–70. doi: 10.1016/j.sab.2013.04.001
- Mikhaylik, Y., Kovalev, I., Schock, R., Kumaresan, K., Xu, J., and Affinito, J. (2010). High energy rechargeable Li-S cells for ev application. *Status Remain. Probl. Solut. ECS Trans.* 25, 23–34. doi: 10.1149/1.3414001
- Miller, D. J., Proff, C., Wen, J. G., Abraham, D. P., and Bareño, J. (2013). Observation of microstructural evolution in Li battery cathode oxide particles by *In Situ* electron microscopy. *Adv. Energy Mater.* 3, 1098–1103. doi: 10.1002/aenm.201300015
- Minami, T., Tatsumisago, M., Wakihara, M., Iwakura, C., Kohjiya, S., and Tanaka, I. (eds.). (2005). *Recent Development of Electrode Materials in Lithium Ion Batteries*. Tokyo: Springer.
- Mohanty, D., Kalnaus, S., Meisner, R. A., Rhodes, K. J., Li, J., Payzant, E. A., et al. (2013). Structural transformation of a lithium-rich Li_{1.2}Co_{0.1}Mn_{0.55}Ni_{0.15}O₂ cathode during high voltage cycling resolved by in situ X-ray diffraction. *J. Power Sour.* 229, 239–248. doi: 10.1016/j.jpowsour.2012.11.144
- Morcrette, M., Chabre, Y., Vaughan, G., Amatucci, G., Leriche, J. B., Patoux, S., et al. (2002). *In situ* X-ray diffraction techniques as a powerful tool to study battery electrode materials. *Electrochim. Acta* 47, 3137–3149. doi: 10.1016/S0013-4686(02)00233-5
- Nelson, J., Misra, S., Yang, Y., Jackson, A., Liu, Y., Wang, H., et al. (2012). In operando X-ray diffraction and transmission X-ray microscopy of lithium sulfur batteries. *J. Am. Chem. Soc.* 134, 6337–6343. doi: 10.1021/ja2121926
- Nishi, T., Nakai, H., and Kita, A. (2013). Visualization of the state-of-charge distribution in a LiCoO₂ cathode by *in situ* raman imaging. *J. Electrochem. Soc.* 160, A1785–A1788. doi: 10.1149/2.061310jes
- Ogata, K., Salager, E., Kerr, C. J., Fraser, A. E., Ducati, C., Morris, A. J., et al. (2014). Revealing lithium–silicide phase transformations in nano-structured silicon-based lithium ion batteries via *in situ* NMR spectroscopy. *Nat. Commun.* 5:3217. doi: 10.1038/ncomms4217
- Ohzuku, T., Takeda, S., and Iwanaga, M. (1999). Solid-state redox potentials for Li[Me₁/2Mn₃/2]O₄ (Me: 3d-transition metal) having spinel-framework structures: a series of 5 volt materials for advanced lithium-ion batteries. *J. Power Sour.* 81–82, 90–94. doi: 10.1016/S0378-7753(99)00246-3
- Ohzuku, T., and Ueda, A. (1994). Solid-State redox reactions of LiCoO (R3m) for 4 volt secondary lithium cells. *J. Electrochem. Soc.* 141, 2972–2977. doi: 10.1149/1.2059267
- Orikasa, A. Y., Maeda, T., Koyama, B. Y., Minato, T., Murayama, H., Fukuda, K., et al. and Ogumi, Z. (2013). Phase transition analysis between LiFePO₄ and FePO₄ by *In-Situ* time-resolved X-ray absorption and X-ray diffraction. *J. Electrochem. Soc.* 160, A3061–A3065. doi: 10.1149/2.012305jes
- Ouvrard, G., Zerrouki, M., Soudan, P., Lestriez, B., Masquelier, C., Morcrette, M., et al. (2013). Heterogeneous behaviour of the lithium battery composite electrode LiFePO₄. *J. Power Sour.* 229, 16–21. doi: 10.1016/j.jpowsour.2012.11.057
- Padhi, A. K., Nanjundaswamy, K. S., and Goodenough, J. B. (1997). Phospho-olivines as positive-electrode materials for rechargeable lithium batteries. *J. Electrochem. Soc.* 144, 1188–1194. doi: 10.1149/1.1837571
- Palacin, M. R. (2009). Recent advances in rechargeable battery materials: a chemist's perspective. *Chem. Soc. Rev.* 38, 2565–2575. doi: 10.1039/b820555h
- Paoella, A., Laul, D., Timoshevskii, V., Zhu, W., Marras, S., Bertoni, G., et al. (2018). The role of metal disulfide interlayer in Li-S batteries. *J. Phys. Chem. C* 122, 1014–1023. doi: 10.1021/acs.jpcc.7b08719
- Paoella, A., Zhu, W., Marceau, H., Kim, C.-S., Feng, Z., Liu, D., et al. (2016). Transient existence of crystalline lithium disulfide Li₂S₂ in a lithium-sulfur battery. *J. Power Sour.* 325, 641–645. doi: 10.1016/j.jpowsour.2016.06.086
- Park, J. H., Cho, J. H., Kim, S. B., Kim, W. S., Lee, S. Y., and Lee, S. Y. (2012). A novel ion-conductive protection skin based on polyimide gel polymer electrolyte: application to nanoscale coating layer of high voltage LiNi_{1/3}Co_{1/3}Mn_{1/3}O₂ cathode materials for lithium-ion batteries. *J. Mater. Chem.* 22, 12574–12581. doi: 10.1039/c2jm16799a
- Patel, M. U., Demir-Cakan, R., Morcrette, M., Tarascon, J. M., Gaberscek, M., and Dominko, R. (2013). Li-S battery analyzed by UV/Vis in operando mode. *ChemSusChem* 6, 1177–1181. doi: 10.1002/cssc.201300142
- Perea, A., Sougrati, M. T., Itonica-Bousquet, C. M., Fraisse, B., Tessier, C., Aldon, L., et al. (2012). Operando 57Fe Mössbauer and XRD investigation of LixMnyFe_{1-y}PO₄/C composites (y = 0.50; 0.75). *RSC Adv.* 2, 9517–9524. doi: 10.1039/C2RA20949G
- Ramana, C. V., Mauger, A., Gendron, F., Julien, C. M., and Zaghbi, K. (2009). Study of the Li-insertion/extraction process in LiFePO₄/FePO₄. *J. Power Sour.* 187, 555–564. doi: 10.1016/j.jpowsour.2008.11.042
- Reimers, J. N., and Dahn, J. R. (1992). Electrochemical and *In Situ* X-Ray diffraction studies of lithium intercalation in LiCoO₂. *J. Electrochem. Soc.* 139, 2091–2097. doi: 10.1149/1.2221184
- Rhodes, K., Meisner, R., Kim, Y., Dudney, N., and Daniela, C. (2011). Evolution of phase transformation behavior in Li(Mn_{1.5}Ni_{0.5})O₄m cathodes studied by *In Situ*, X. R. D. *J. Electrochem. Soc.* 158, A890–A897. doi: 10.1149/1.3596376
- Roberts, M. R., Madsen, A., Nicklin, C., Rawle, J., Palmer, M. G., Owen, J. R., et al. (2014). Direct observation of active material concentration gradients and crystallinity breakdown in LiFePO₄ electrodes during charge/discharge cycling of lithium batteries. *J. Phys. Chem. C* 118, 6548–6557. doi: 10.1021/jp411152s
- Samarasingha, P., Sottmanna, J., Margadonna, S., and Fjellvåga, H. (2016). *In situ* synchrotron study of ordered and disordered LiMn_{1.5}Ni_{0.5}O₄ as lithium ion battery positive electrode. *Acta Mater.* 116, 290–297. doi: 10.1016/j.actamat.2016.06.040
- Saravanan, K., Jarry, A., Kostecki, R., and Chen, G. (2015). A study of room-temperature LixMn_{1.5}Ni_{0.5}O₄ solid solutions. *Sci. Rep.* 5:8027. doi: 10.1038/srep08027
- Sarkar, S., and Mitra, S. (2014). Carbon coated submicron sized-LiFePO₄: improved high rate performance lithium battery cathode. *Energy Proc.* 54, 718–724. doi: 10.1016/j.egypro.2014.07.312
- Shin, H. C., Chung, K. Y., Min, W. S., Byun, D. J., Jang, H., and Cho, B. W. (2008). Asymmetry between charge and discharge during high rate cycling in LiFePO₄ – *in situ* X-ray diffraction study. *Electrochem. Commun.* 10, 536–540. doi: 10.1016/j.elecom.2008.02.002
- Shin, H. C., Nam, K. W., Chang, W. Y., Cho, B. W., Yoon, W.-S., Yang, X.-Q., et al. (2011). Comparative studies on C-coated and uncoated LiFePO₄ cycling at various rates and temperatures using synchrotron based in situ X-ray diffraction. *Electrochim. Acta* 56, 1182–1189. doi: 10.1016/j.electacta.2010.10.087
- Siddique, N. A., Salehi, A., Wei, Z., Liu, D., Sajjad, S., and Liu, F. (2015). Length-Scale-Dependent Phase transformation of LiFePO₄ an *In situ* and operando study using Micro-Raman spectroscopy and XRD. *Chemphyschem* 16, 2383–2388. doi: 10.1002/cphc.201500299
- Stancovski, V., and Badilescu, S. (2013). *In situ* Raman spectroscopic-electrochemical studies of lithium-ion battery materials: a historical overview. *J. Appl. Electrochem.* 44, 23–43. doi: 10.1007/s10800-013-0628-0

- Sun, X., Yang, X. Q., Mcbreen, J., Gao, Y., Yakovleva, M. V., Xing, X. K., et al. (2001). New phases and phase transitions observed in over-charged states of LiCoO₂-based cathode materials. *J. Power Sour.* 97–98, 274–276. doi: 10.1016/S0378-7753(01)00512-2
- Sun, Y., Zhao, L., Pan, H., Lu, X., Gu, L., Hu, Y. S., et al. (2013). Direct atomic-scale confirmation of three-phase storage mechanism in Li₄Ti₅O₁₂ anodes for room-temperature sodium-ion batteries. *Nat. Commun.* 4:1870. doi: 10.1038/ncomms2878
- Takahashi, K., Saitoh, M., Sano, M., Fujita, M., and Kifune, K. (2004). Electrochemical and structural properties of a 4.7 V-Class LiNi_{0.5}Mn_{1.5}O₄ positive electrode material prepared with a self-reaction method. *J. Electrochem. Soc.* 151, A173–A177. doi: 10.1149/1.1633267
- Tarascon, J. M., and Armand, M. (2001). Issues and challenges facing rechargeable lithium batteries. *Nature* 414, 359–367. doi: 10.1038/35104644
- Waluś, S., Barchasz, C., Colin, J. F., Martin, J. F., Elkaim, E., Leprêtre, J. C., et al. (2013). New insight into the working mechanism of lithium-sulfur batteries: in situ and operando X-ray diffraction characterization. *Chem. Commun. (Camb.)* 49, 7899–7901. doi: 10.1039/c3cc43766c
- Wang, C. M. (2015). *In situ* transmission electron microscopy and spectroscopy studies of rechargeable batteries under dynamic operating conditions: a retrospective and perspective view. *J. Mater. Res.* 30, 326–339. doi: 10.1557/jmr.2014.281
- Wang, H., and Wang, F. (2016). *In situ*, operando measurements of rechargeable batteries. *Curr. Opin. Chem. Eng.* 13, 170–178. doi: 10.1016/j.coche.2016.09.002
- Wang, L., Li, H., Huang, X., and Baudrin, E. (2011). A comparative study of Fd-3m and P4332 “LiNi_{0.5}Mn_{1.5}O₄”. *Solid State Ionics* 193, 32–38. doi: 10.1016/j.ssi.2011.04.007
- Wang, X. L., An, K., Cai, L., Feng, Z., Nagler, S. E., Daniel, C., et al. (2012). Visualizing the chemistry and structure dynamics in lithium-ion batteries by *in-situ* neutron diffraction. *Sci. Rep.* 2:747. doi: 10.1038/srep00747
- Wen, J., Yu, Y., and Chen, C. (2012). A review on lithium-ion batteries safety issues: existing problems and possible solutions. *Mater. Express* 2, 197–212. doi: 10.1166/mex.2012.1075
- Wu, H. L., Huff, L. A., and Gewirth, A. A. (2015). *In situ* Raman spectroscopy of sulfur speciation in lithium-sulfur batteries. *ACS Appl. Mater. Interfaces* 7, 1709–1719. doi: 10.1021/am5072942
- Wu, J., Dathar, G. K., Sun, C., Theivanayagam, M. G., Applestone, D., Dylla, A. G., et al. (2013). *In situ* Raman spectroscopy of LiFePO₄: size and morphology dependence during charge and self-discharge. *Nanotechnology* 24:9. doi: 10.1088/0957-4484/24/42/424009
- Xu, Z.-L., Cao, K., Abouali, S., Akbari Garakani, M., Huang, J., Huang, J.-Q., et al. (2016). Study of lithiation mechanisms of high performance carbon-coated Si anodes by *in-situ* microscopy. *Energy Storage Mater.* 3, 45–54. doi: 10.1016/j.ensm.2016.01.003
- Yang, J., Han, X., Zhang, X., Cheng, F., and Chen, J. (2013). Spinel LiNi_{0.5}Mn_{1.5}O₄ cathode for rechargeable lithium-ion batteries: nano vs micro, ordered phase (P4332) vs disordered phase (Fd3-m). *Nano Res.* 6, 679–687. doi: 10.1007/s12274-013-0343-5
- Yang, S., He, P., and Zhou, H. (2018). Research progresses on materials and electrode design towards key challenges of Li-air batteries. *Energy Storage Mater.* 13, 29–48. doi: 10.1016/j.ensm.2017.12.020
- Yang, X. Q., Mcbreen, J., Yoon, W.-W., and Grey, C. P. (2002). Crystal structure changes of LiMn_{0.5}Ni_{0.5}O₂ cathode materials during charge and discharge studied by synchrotron based *in situ* XRD. *Electrochem. Commun.* 4, 649–654. doi: 10.1016/S1388-2481(02)0406-X
- Yang, X. Q., and Nam, K. W. (2010). *In situ* Characterizations of New Battery Materials and the Studies of High Energy Density Li-Air Batteries. PPT.
- Yang, X. Q., Sun, X., and Mcbreen, J. (2000). New phases and phase transitions observed in Li_{1-x}CoO₂ during charge: *in situ* synchrotron X-ray diffraction studies. *Electrochem. Commun.* 2, 100–103. doi: 10.1016/S1388-2481(99)00155-1
- Ye, J.-Y., Jiang, Y.-X., Sheng, T., and Sun, S.-G. (2016). *In-situ* FTIR spectroscopic studies of electrocatalytic reactions and processes. *Nano Energy* 29, 414–427. doi: 10.1016/j.nanoen.2016.06.023
- Yeon, J. T., Jang, J. Y., Han, J. G., Cho, J., Lee, K. T., and Choi, N. S. (2012). Raman spectroscopic and X-ray diffraction studies of sulfur composite electrodes during discharge and charge. *J. Electrochem. Soc.* 159, A1308–A1314. doi: 10.1149/2.080208jes
- Zhang, X., Kuhnle, R.-S., Schroeder, M., and Balducci, A. (2014). Revisiting Li₃V₂(PO₄)₃ as an anode – an outstanding negative electrode for high power energy storage devices. *J. Mater. Chem. Phys.* 2, 17906–17913. doi: 10.1039/C4TA03845B
- Zhao, N., Li, Y., Zhi, X., Wang, L., Zhao, X., Wang, Y., et al. (2016). Effect of Ce³⁺ doping on the properties of LiFePO₄ cathode material. *J. Rare Earths* 34, 174–180. doi: 10.1016/S1002-0721(16)60011-X
- Zhu, W., Liu, D., Trottier, J., Gagnon, C., Guerfi, A., Julien, C. M., et al. (2014). Comparative studies of the phase evolution in M-doped Li_xMn_{1.5}Ni_{0.5}O₄ (M = Co, Al, Cu and Mg) by *in-situ* X-ray diffraction. *J. Power Sour.* 264, 290–298. doi: 10.1016/j.jpowsour.2014.03.122
- Zhu, W., Liu, D., Trottier, J., Gagnon, C., Howe, J., Mauger, A., et al. (2015). *In-situ* Raman spectroscopic investigation of LiMn_{1.45}Ni_{0.45}M_{0.10}O₄ (M = Cr, Co) 5 V cathode materials. *J. Power Sour.* 298, 341–348. doi: 10.1016/j.jpowsour.2015.07.083
- Zhu, W., Liu, D., Trottier, J., Gagnon, C., Mauger, A., Julien, C. M., et al. (2013). *In-situ* X-ray diffraction study of the phase evolution in undoped and Cr-doped Li_xMn_{1.5}Ni_{0.5}O₄ (0.1 < x < 1.0) 5-V cathode materials. *J. Power Sources* 242, 236–243. doi: 10.1016/j.jpowsour.2013.05.021
- Zhu, W., Paoletta, A., Kim, C.-S., Liu, D., Feng, Z., Gagnon, G., et al. (2017). Investigation of the reaction mechanism of lithium sulfur batteries in different electrolyte systems by *in situ* Raman spectroscopy and *in situ* X-ray diffraction. *Sustain. Energy Fuels* 1, 737–747. doi: 10.1039/C6SE00104A
- Zhu, Y., Wang, J. W., Liu, Y., Liu, X., Kushima, A., Liu, Y., et al. (2013). *In Situ* atomic-scale imaging of phase boundary migration in fepo 4 microparticles during electrochemical lithiation. *Adv. Mater. Weinheim.* 25, 5461–5466. doi: 10.1002/adma.201301374

Conflict of Interest Statement: The authors declare that the research was conducted in the absence of any commercial or financial relationships that could be construed as a potential conflict of interest.

Copyright © 2018 Zhu, Liu, Paoletta, Gagnon, Gariépy, Vijn and Zaghieb. This is an open-access article distributed under the terms of the Creative Commons Attribution License (CC BY). The use, distribution or reproduction in other forums is permitted, provided the original author(s) and the copyright owner(s) are credited and that the original publication in this journal is cited, in accordance with accepted academic practice. No use, distribution or reproduction is permitted which does not comply with these terms.